

NAVAL POSTGRADUATE SCHOOL

Monterey, California

AD-A237 100



DTIC
ELECTED
JUN 24 1991
S B D

THESIS

Acoustic Tomographic Estimate of
Ocean Advection Heat Flux:
A Numerical Assessment in the Norwegian Sea

by

Richard Timothy Barock

June 1990

Thesis Advisor:
Co-advisor:

Ching-Sang Chiu
James H. Miller

Approved for public release; distribution unlimited.

91-02865



Unclassified

Security Classification of this page

REPORT DOCUMENTATION PAGE

1a Report Security Classification Unclassified			1b Restrictive Markings		
2a Security Classification Authority			3 Distribution Availability of Report Approved for public release; distribution is unlimited.		
2b Declassification/Downgrading Schedule					
4 Performing Organization Report Number(s)			5 Monitoring Organization Report Number(s)		
6a Name of Performing Organization Naval Postgraduate School			7a Name of Monitoring Organization Naval Postgraduate School		
6c Address (city, state, and ZIP code) Monterey, CA 93943-5000			7b Address (city, state, and ZIP code) Monterey, CA 93943-5000		
8a Name of Funding/Sponsoring Organization			9 Procurement Instrument Identification Number		
8c Address (city, state, and ZIP code)			10 Source of Funding Numbers		
			Program Element Number	Project No	Task No
					Work Unit Accession No
11 Title (<i>Include Security Classification</i>) Acoustic Tomographic Estimate of Ocean Advective Heat Flux: A Numerical Assessment in the Norwegian Sea					
12 Personal Author(s) Barock, Richard Timothy					
13a Type of Report Master's Thesis		13b Time Covered From To		14 Date of Report (year, month, day) June 1990	
16 Supplementary Notation The views expressed in this thesis are those of the author and do not reflect the official policy or position of the Department of Defense or the U.S. Government.					
17 Cosati Codes		18 Subject Terms (<i>continue on reverse if necessary and identify by block number</i>) Acoustic Tomography, Ocean Heat Flux			
19 Abstract (<i>continue on reverse if necessary and identify by block number</i> In a computer simulation experiment, acoustic tomography is assessed as a means of measuring the seasonal flux of heat advected by the Norwegian Atlantic Current. Oceanic heat flux has traditionally been measured by various direct or indirect techniques that are prone to error or large uncertainty. The tomographic technique offers distinct advantages over conventional methods in that temperature and current fields, that combine to yield heat flux in the ocean, can be determined at various spatial and temporal scales. The adequacy of the tomographic technique thus hinges on the question of "how well can the temperature and current be resolved spatially?" The spatial resolution of tomography varies with array size, number of transceivers used and the characteristics of the sound channel.					

In the assessment we use the General Digital Environmental Model (GDEM), a climatological data base, to simulate an ocean area 550 x 550 km² off the Norwegian Coast. Resolution and variance analysis are performed on two circular arrays consisting of six transceivers. An important finding is that the horizontal resolution lengths of the current and temperature fields differ. For a six element array the horizontal resolution length is approximately one fifth the array diameter for the current field, whereas for the temperature field it is one sixth the array diameter.

20 Distribution/Availability of Abstract <input checked="" type="checkbox"/> unclassified/unlimited <input type="checkbox"/> same as report <input type="checkbox"/> DTIC users			21 Abstract Security Classification Unclassified		
22a Name of Responsible Individual Ching-Sang Chiu			22b Telephone (<i>Include Area code</i>) (408) 646-3239		
DD FORM 1473, 84 MAR			22c Office Symbol Oc/Ci		
83 APR edition may be used until exhausted All other editions are obsolete					
security classification of this page Unclassified					

Unclassified

Security Classification of this page

We then generate synthetic travel time data that have embedded within them temperature and current signals as well as random noise. We invert the synthetic travel time data to form estimates of the original fields using a linear optimal estimator based on the Gauss-Markoff theorem. We relate the sound speed perturbation field to potential temperature and compare these estimates to the original values. Finally we use the estimated fields to compute heat flux across a transect located within the array. We compare the actual to the estimated heat flux to asses the quality of the tomographically derived value. We have found that the quality of the heat flux estimates depends critically on how well the flow field is resolved. A six element array can adequately resolve the current in the Norwegian Sea, provided that its diameter is shorter than 250 km. Such an array is able to measure net heat flux through a transect at the center of the array with only a 10% error.

Accession For	
NTIS GRA&I	<input checked="" type="checkbox"/>
DTIC TAB	<input type="checkbox"/>
Unannounced	<input type="checkbox"/>
Justification	
By _____	
Distribution/	
Availability Codes	
Dist	Avail and/or Special
A-1	



S/N 0102-LF-014-6601

Security Classification of this page

Unclassified

Approved for public release; distribution is unlimited.

**Acoustic Tomographic Estimate of Ocean Advective Heat Flux:
A Numerical Assessment in the Norwegian Sea**

by

**Barock, Richard Timothy
Lieutenant Commander, U. S Navy
M.S., University of Southern California, 1985
B.S., University of Notre Dame, 1978**

Submitted in partial fulfillment of the requirements for
the degree of

**MASTER OF SCIENCE IN OCEANOGRAPHY AND
METEOROLOGY**

from the

**NAVAL POSTGRADUATE SCHOOL
June 1990**

Author:

Richard Timothy Barock
Richard Timothy Barock

Approved by:

C. C. Chiu
Ching-Sang Chiu
Thesis Advisor

J. H. Miller
James H. Miller
Thesis Co-advisor

E. B. Thompson
Curtis A. Collins
Chairman, Department of Oceanography

ABSTRACT

In a computer simulation experiment, acoustic tomography is assessed as a means of measuring the seasonal flux of heat advected by the Norwegian Atlantic Current. Oceanic heat flux has traditionally been measured by various direct or indirect techniques that are prone to error or large uncertainty. The tomographic technique offers distinct advantages over conventional methods in that temperature and current fields, that combine to yield heat flux in the ocean, can be determined at various spatial and temporal scales. The adequacy of the tomographic technique thus hinges on the question of "how well can the temperature and current be resolved spatially?" The spatial resolution of tomography varies with array size, number of transceivers used and the characteristics of the sound channel.

In the assessment we use the General Digital Environmental Model (GDEM), a climatological data base, to simulate an ocean area $550 \times 550 \text{ km}^2$ off the Norwegian Coast. Resolution and variance analysis are performed on two circular arrays consisting of six transceivers. An important finding is that the horizontal resolution lengths of the current and temperature fields differ. For a six element array the horizontal resolution length is approximately one fifth the array diameter for the current field , whereas for the temperature field it is one sixth the array diameter.

We then generate synthetic travel time data that have embedded within them temperature and current signals as well as random noise. We invert the synthetic travel time data to form estimates of the original fields using a linear optimal estimator based on the Gauss-Markoff theorem. We relate the sound speed

perturbation field to potential temperature and compare these estimates to the original values. Finally we use the estimated fields to compute heat flux across a transect located within the array. We compare the actual to the estimated heat flux to asses the quality of the tomographically derived value. We have found that the quality of the heat flux estimates depends critically on how well the flow field is resolved. A six element array can adequately resolve the current in the Norwegian Sea, provided that its diameter is shorter than 250 km. Such an array is able to measure net heat flux through a transect at the center of the array with only a 10% error.

TABLE OF CONTENTS

I. INTRODUCTION.....	1
A. PURPOSE	1
B. APPROACH.....	3
C. BACKGROUND	6
1. Oceanic Heat Flux Measurement.....	6
a. Direct Methods	7
b. Indirect Methods.....	8
2. Tomography Overview.....	10
a. Travel Time.....	11
b. Tomographic Estimate of Heat Flux.....	13
3. Environment.....	13
a. Dominant Flow.....	15
b. Bathymetry	15
c. Fronts.....	16
d. Ice	16
e. Acoustic Properties.....	17
f. Summary.....	19
II. PHYSICS OVERVIEW.....	20
A. TOMOGRAPHIC FORWARD MODELING	20
1. Time of Flight.....	20
a. Density Tomography.....	21
b. Current Tomography	22
2. Experimental Noise	22

B. A DISCRETE STOCHASTIC INVERSE METHOD.....	23
1. Discretization of an Ocean Volume	23
2. Gauss-Markoff Estimate.....	23
3. Covariance Functions.....	24
4. Error.....	25
5. Resolution	27
6. Heat flux estimate and error.....	30
C. SUMMARY.....	31
III. NUMERICAL OCEAN AND ARRAY SIMULATIONS.....	33
A. SYNTHETIC OCEAN.....	33
1. Spatial Resolution.....	33
2. Bathymetry	34
3. GDEM Data Base.....	34
4. Model Parameters.....	34
5. Acoustic Environment	39
B. ARRAY GEOMETRY	39
C. RAY TRACING.....	40
D. SYNTHETIC TRAVEL TIME DATA.....	42
E. INVERSION	42
F. RESOLUTION	42
IV. RESULTS AND DISCUSSION.....	44
A. RESOLUTION	45
1. Sound speed perturbation field.....	45
2. Current field	50
B. ERROR.....	59
1. Actual vs. Estimated Fields.....	59
a. Theta.....	59
b. Current estimates.....	61
2. Predicted RMS Error	65

a. Predicted error of the sound speed field.....	65
b. Predicted error of the current estimate	65
C. HEAT FLUX ESTIMATES.....	72
1. Point estimates.....	72
2. Depth Integrated estimates.....	78
3. Heat Flux Through a Transect.....	82
V. CONCLUSIONS.....	86
A. SUMMARY.....	86
1. Covariance of the Solution.....	86
2. Acoustic Channel and Vertical Resolution.....	87
3. Array Geometry and Horizontal Resolution	87
4. Comparison with Conventional Techniques.....	87
5. Viability of the technique	88
B. CONCLUSIONS.....	88
REFERENCES	90
INITIAL DISTRIBUTION LIST.....	92

LIST OF NOTATION

A	Matrix of forward transfer function (nxm) for sound speed
B	Matrix of forward transfer function (nxm) for current
b	Bias error in the sound speed perturbation estimate
C_{δc}	Covariance matrix of sound speed perturbation (nxn)
C_ε	Covariance matrix of error in the sound speed perturbation estimate (nxn)
C_e	Covariance matrix of random noise in the travel time perturbation data (mxm)
C_{ε'}	Covariance matrix of random noise in the travel time difference data (mxm)
C_η	Covariance matrix of error in the current estimate (nxn)
C_y	Covariance matrix of current (nxn)
c₀	Background sound speed
c_p	Specific Heat of seawater
d	Bias error in the current estimate
δc	Sound speed perturbation field
δĉ	Vector discretization of δc (n x 1)
δĉ̂	Estimate of δc
δT_i	Travel time perturbation along Path i
δT̂_i	Difference in reciprocal travel times perturbations along the ith Path

δT	Vector (mx1) containing all the travel time perturbation data
δT^-	Vector (mx1) containing all the travel time difference data
E_i	Total energy of the i th resolution kernel \mathbf{r}_i^T
ϵ	Noise in δT
ϵ'	Noise in δT^-
F_x, F_y	Zonal and meridional components of heat flux
H	Height limit of a transect
H_x, H_y	Horizontal resolution length in the zonal and meridional directions, respectively
L_x, L_y	Horizontal correlation lengths of the unknown field in the zonal and meridional directions
L_z	Vertical correlation length of the unknown field
σ_v	The rms value of the current
$\sigma_{\delta c}$	The rms value of the sound speed perturbation field
T_i	Time of flight of an acoustic pulse in the absence of δc and \vec{V}
δT_i	Change of time due to the presence of δc and \vec{V}
t	Ocean temperature in degrees Celsius
θ	Ocean thermodynamic temperature
R, \mathbf{r}_i^T	Resolution matrix ($n \times n$) and the i th resolution kernel vector (nx1), respectively
ρ	Density of seawater
s	Arc length of an acoustic ray
U, V	The left singular value matrix (mxm) and right singular value matrix ($n \times n$) in a singular value decomposition of A .

Q,S The left singular value matrix (mxm) and right singular value matrix (nxn) in a singular value decomposition of **B**.

u_i, v_i ith and jth columns of **U** and **V** respectively.

q_i, s_i ith and jth columns of **Q** and **S** respectively.

Λ, λ_i Matrix(mxn) containing singular values and the ith diagonal element (singular value), respectively.

P, φ_i Matrix(mxn) containing singular values and the ith diagonal element (singular value), respectively.

vec Ocean current vector.

V_x Zonal component of current.

V_y Meridional component of current.

V Vector discretization of **vec** (2nx1).

hat{V} Estimate of V (2nx1)

ACKNOWLEDGMENTS

I would like to express my sincere thanks to the Ocean Modeling Division at Fleet Numerical Oceanography Center who provided the General Digital Environmental Data, GDEM climatology that made this numerical simulation possible. Most helpful were Mike Clancy and Ken Pollak who assisted with the code to retrieve the data and Mike Corcoran who assisted with the conversion of CDC binary format into a more generic ASCII code.

My acknowledgement would not be complete without recognizing Dennis Mar and Laura Ehret for their assistance with the IMSL code used to map the irregularly spaced GDEM data into a regularly spaced Cartesian coordinate system. Additionally, Craig Motell and Professor Wendell Nuss rendered invaluable assistance in the use of NCAR graphics which were used to present the results of this simulation. I would also like to acknowledge Russ Schwantz and Donna Burych for their cheerful support in fielding VAX questions and keeping the system up and running.

I would also like to thank my advisors Professors Chiu and Miller for inviting me to join in their research, in the new and challenging field of acoustic tomography. They were a constant source of encouragement and enlightenment. They have allowed me to experience the thrill and satisfaction that result from scientific inquiry. Their hours of patient counsel, and guidance enabled me to form and express the concepts herein. Without their guidance and assistance none of this would have been possible.

Finally, I would like to thank my wife, Susan for her love, support, and understanding during the course of these challenging pursuits; and to the Good Lord for sharing with us the wonders of his creation.

I. INTRODUCTION

Ocean acoustic tomography is a technique that uses a fixed array of transceivers to measure travel times of pulses along acoustic multi-paths. These measurements contain the information necessary to allow determination of temperature $t(x,y,z,t)$ and current $V(x,y,z,t)$ structure. The concept was first introduced by Munk and Wunsch (1979) as a means of large scale monitoring of mesoscale processes occurring in the ocean. Since that time acoustic tomography has become a viable tool for measuring the oceans physical properties and has greatly enhanced our ability to probe beneath the ocean surface. Ocean acoustic tomography has been successfully demonstrated in a variety of applications such as the mapping of a mesoscale eddy field by Cornuelle *et al* (1983), planetary wave analysis by Chiu and Desaubies (1987) and surface wave spectra analysis by Lynch *et al* (1987). This thesis explores yet another application of ocean acoustic tomography, namely the measurement of ocean advective heat flux.

A. PURPOSE

The world's oceans play a major role in the redistribution of energy to maintain the earth in thermal balance. The equatorial regions of the earth receive a net excess of energy from insolation while the poles lose more than they receive. Excess energy at the equator that cannot be reradiated back into space must be advected away by the atmosphere and ocean to maintain a local thermal equilibrium. The net energy flux is poleward over the entire globe. Many attempts have been made over the past four decades to accurately compute ocean heat

flux. According to Vonder Haar and Oort (1973), the oceans are responsible for up to 40% of the heat flux. However past measurements of the oceans contribution have been in error by as much as 70%. The poleward flux of heat has a governing effect on several processes including, ocean circulation, weather, climate and formation of ice in the arctic. Being able to accurately measure ocean heat flux is the first step in being able to model and predict these processes that influence the habitability of our planet.

Ocean flux measurement has always been hard to accomplish primarily due to the difficulty in sampling the oceans temperature and current structure on adequate temporal and spatial scales. Acoustic tomography has a potential for overcoming this limitation. In this study, we shall assess the adequacy of a tomographic technique for estimating ocean heat flux through simulated arrays in an area off the Norwegian Coast. This region is influenced primarily by the flow of the Norwegian Atlantic Current.

The Norwegian Atlantic Current forms a conduit for the poleward flux of relatively warm, saline, North Atlantic water along the Norwegian coast shown in Figure 1-1. This three Sverdrup¹ (Sv) flow branches into an easterly flowing North Cape Current, and the poleward flowing, West Spitsbergen Current. These currents help to mediate the advance and retreat of the ice pack in the Marginal Ice Zone. A tomographic array located in this region could in principle allow for the monitoring of oceanic heat flux into the Barents Sea and the Arctic basin.

¹ Sverdrup is the unit of mass transport, $1 \text{ Sv} = 10^6 \text{ meters}^3 \text{ sec}^{-1}$

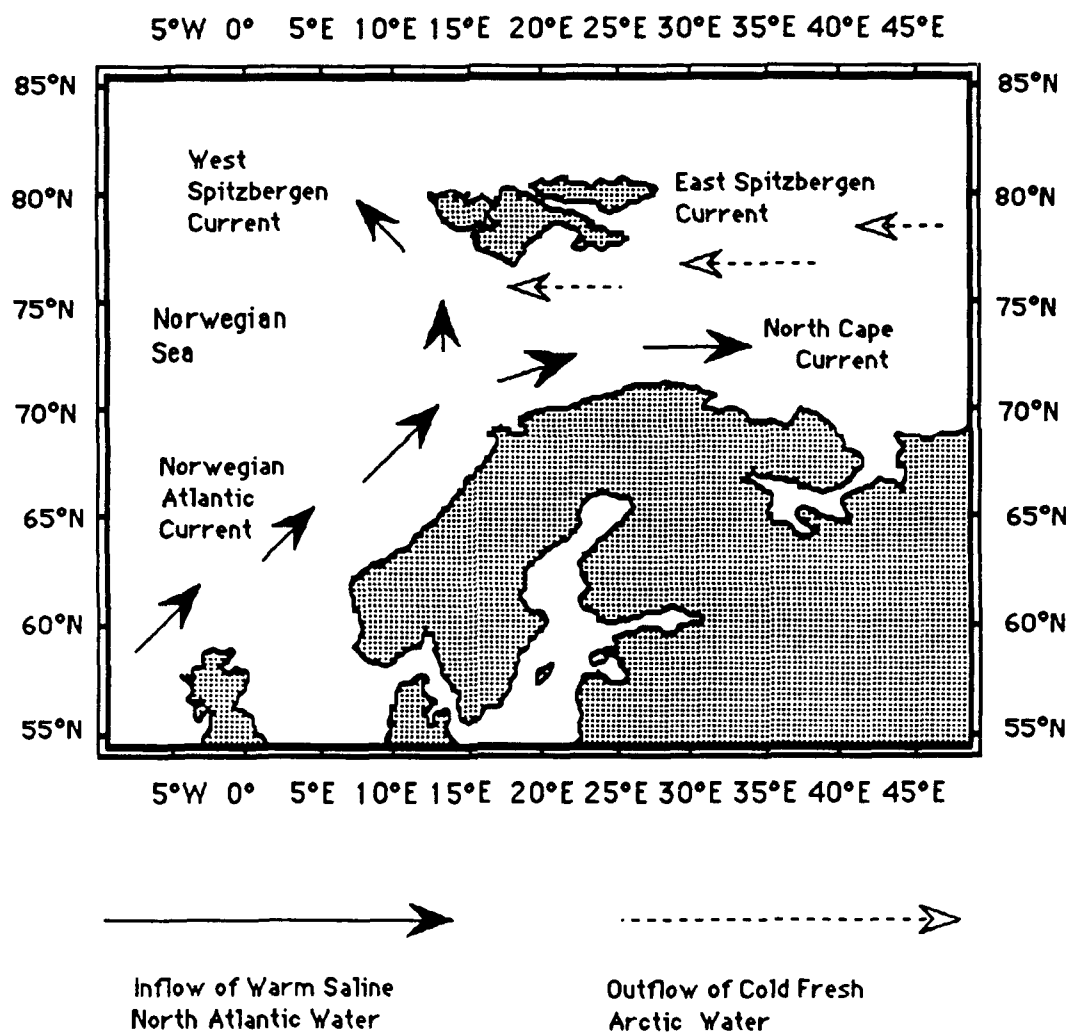


Figure 1-1 Geography: Overview of the Current System of the Nordic Sea Region.

B. APPROACH

Our assessment begins with a review of some techniques for estimating ocean heat flux that have been used in the past. We then assess the tomographic method by performing simulation inversions of synthetic acoustic travel time data computed from sound speed and current fields derived from climatological

temperature and salinity information. Separate inversions of the changes and differences of reciprocal path travel times will allow us to construct independent estimates of temperature and current throughout the volume surrounded by the array. From these tomographic products we then construct the zonal and meridional estimates of heat flux. We compare the tomographic estimates of temperature, current, and heat flux with the actual values of these parameters as a means of assessing performance of the technique. The central issue in this study is, how well tomography can resolve the temperature and the current fields in the ocean, the basic parameters of heat flux calculations. Of particular interest is the quality of the current estimate both in magnitude and direction.

We have selected climatology from the General Digital Environmental Model (GDEM) data base with the intent of modeling a region in the upper Norwegian Sea off the coast of Norway. The model domain lies in the path of the poleward flowing Norwegian Atlantic current. The GDEM data cover two separate months that represent seasonal extremes of summer and winter, in a region bounded by 5° - 20° East and 67° - 72° North. These two data sets provide the ocean environment for our acoustic simulations.

Our GDEM data base consists of climatological temperature and salinity profiles at half degree horizontal resolution. We derive sound velocity and potential temperature fields based on empirical expressions using the GDEM temperature and salinity fields. We also derive current fields based on geostrophy. These derived fields form the truth data in our numerical simulation.

Additionally, we perform resolution and variance analysis at five depths for both the sound speed perturbation and the current field. These statistical analyses require no data and they provide us with quantitative measures of how well a

given array geometry resolves the ocean temperature and current structure. The geometries include a large and a small circular array with diameters of 525 and 250 km respectively. The smaller array contains about 25% of the area of the larger array. We would like to determine how much area can be covered by a six element array and still adequately measure heat flux.

We invert the synthetic travel time data obtained from original sound speed perturbation and current fields to derive estimates of the sound speed perturbation field and current field. We then convert the sound speed perturbation estimate into a potential temperature field using a technique explained in the next Chapter. Using the potential temperature and current fields, point estimates are made for zonal and meridional flux over the model domain. In addition, we compute depth integrated estimates and zonal and meridional heat flux through a transect inside the array. Estimated values of all the parameters are compared with actual model values to assess the quality of each estimate.

An outline of the remainder of the thesis follows. In the balance of this chapter we provide a comparative summary of conventional techniques that have been used in ocean heat flux estimates. Additionally, we discuss the proposed tomographic method, and the details of how we intend to use it to derive heat flux values. Finally, we discuss the environmental factors that are likely to affect the performance of a tomographic array in the upper Norwegian Sea.

In Chapter II, we discuss the forward and inverse problems for both density and current tomography. In particular, we discuss how to construct inverse solutions, using the Gauss-Markoff estimator, and perform resolution and variance analysis that is used to quantify tomographic array performance. We also discuss the estimation of heat flux from standard tomographic products,

sound speed and current maps. In Chapter III, we describe in detail the numerical experiment including ocean simulation, array simulation, and the creation of synthetic travel time data for the inversion. Chapter IV contains the results and discussion of the experiment. Finally in Chapter V, we summarize our results and presents our conclusions.

C. BACKGROUND

1. Oceanic Heat Flux Measurement

Heat flux is a quantitative description of the movement of heat through a surface from one region to another expressed in units of power (watts). The total heat budget for the earth can be viewed as the sum of various terms representing sources and sinks. Historically, the approach has been to assume that the earth is in thermal equilibrium so that the net energy gain in time is zero. This is expressed in Equation (1.1).

$$\begin{aligned} [\text{Net Gain}] &= [\text{Source}] - [\text{Sink}] - [\text{Advection}] \\ Q_{\text{Net}} &= [Q_S - Q_R] - [Q_B + Q_E + Q_H] - [Q_{VA} + Q_{VO}] \quad (1.1) \end{aligned}$$

where:

Q_{Net} = Net heat gain or loss in time.

Q_S = Heat source due to insolation.

Q_R = Heat loss due to reflective albedo.

Q_B = Heat loss due to long wave radiation.

Q_E = Heat loss due to latent heat of vaporization.

Q_H = Heat gain due to precipitation.

Q_{VA} = Heat loss due to atmospheric flux.

Q_{VO} = Heat loss due to ocean flux.

Average values of the source and sink terms in the heat balance equation can be measured with modest accuracy. Measuring the advection terms [$Q_{VA} + Q_{VO}$], is a more difficult problem. Early researchers calculated the ocean advection of heat as a small residual of the difference between the very large source and sink terms (Sverdrup, 1957). This calculation had large uncertainty and could not resolve the controversy over the relative importance of the atmosphere and ocean in the flux of heat from the equator. The requirement for a steady state and a bounded system did not easily lend itself to the study of regional or local heat flux problems. This technique was ultimately abandoned in favor of more precise methods.

The appearance of satellites and the refinement of other in situ sensing devices such as current meters led to the development of measurement techniques that can be divided into two general classes, namely the direct and indirect methods. The technology that made these methods possible marked a considerable improvement in the ability to calculate ocean thermal flux.

a. Direct Methods

As the name implies, the direct method simply uses direct measurement of the components that make up heat flux in the ocean. These components are potential temperature θ (K°), and current V (meters sec $^{-1}$), perpendicular to an arbitrary boundary. The general Equation (1.2) is given by Bryan (1962).

$$Q_{VO} = \int_0^L \int_{-H}^0 \rho C_p \theta V_\perp dz dx \quad (1.2)$$

Heat flux can be broken down into a product of the temperature and velocity

field perpendicular to a boundary that the heat is being advected through ; where L is the length of the boundary, in meters , H is the height in meters, C_p (Joules $\text{kg}^{-1}\text{K}^{\circ-1}$) is the specific heat of seawater at constant pressure and ρ (kg meter^{-3}) is the density of seawater.

Since much of the temperature variability of the ocean lies above the thermocline, temperature fields can be constructed over broad ocean areas based on satellite sea surface temperature maps and several well positioned in situ measurements of the water column as shown by Oort and Vonder Haar (1976). If satellite data are not available, then direct measurements must be made by conventional ocean survey techniques which are laborious, time consuming and expensive.

Velocity fields are more difficult to measure by direct means and a variety of techniques have been developed. The most common method is to assume that currents are geostrophic. The ageostrophic component is assumed to be negligible and for large scale, or climatological studies, this is generally true. In local and regional studies, the ageostrophic component may be significant. In these cases, other techniques may be necessary if available. Other techniques include Eulerian methods involving the deployment of fixed current meters and Lagrangian methods that feature sensors moving with the flow that are tracked by sonar or aerial reconnaissance. These methods have varying degrees of success but each bears a heavy price for coverage and spatial resolution. Thus the geostrophic technique remains a popular choice.

b. Indirect Methods

Two independent methods have been used for indirect heat flux measurement, namely the air-sea exchange and the satellite radiation method.

The first method is based on the measurement of air-sea fluxes of momentum, water vapor, sensible heat and radiation based on bulk aerodynamic and radiation equations. The bulk formulas require coefficients that are derived empirically. Once the surface fluxes between the air and sea are determined these values are integrated over an area poleward of a given latitude. Positive fluxes (air to sea) occur at the equator, while negative fluxes (sea to air) occur in the polar regions. Heat flux is then calculated by assuming that the deficit in the integrated region above a given latitude is exactly balanced by a flux of poleward energy across that latitude. A detailed discussion of this method is provided by Bunker (1976). An application of this method in the Polar region is given in Mosby (1962).

A second method is based on the use of satellite radiation data. Using this technique, ocean heat flux is calculated as a residual between the net incoming and outgoing radiation utilizing the assumptions of Equation (1.1). In this method satellite data must be averaged in time and space, and energy storage by the ocean and atmosphere is assumed to be negligible. Atmospheric heat flux is calculated directly from observations. Ocean flux is then calculated as the difference between the total advection and the atmospheric component

$$Q_{VOcean} = Q_{VTotal} - Q_{VAir}.$$

The preferred method of computing ocean heat flux is the direct method. The method features simplicity and error depends only on how well temperature and velocity are measured. The assumptions of a steady state system and closed boundaries are unnecessary. Unfortunately temperature and in particular velocity are not well resolved over large areas using conventional measuring techniques and thus the direct method is costly, time consuming, and offers only limited coverage.

Indirect measurements have the advantage of providing global coverage of ocean heat flux. However error can be introduced as in the bulk aerodynamic method by the uncertainty of the exchange coefficients that are required in these calculations. In addition, many more measurements must be taken to compute the various terms required by this technique. This can lead to greater error unless the data is carefully averaged. The satellite radiation method features excellent areal coverage, but also has some limitations. Diurnal sampling and sensor calibration errors, spatial gaps and uncertainties in the value of the solar constant can all adversely influence satellite radiation measurements. A further drawback is that atmospheric heat flux is not well resolved over the oceans due to the sparseness of data, particularly in the southern hemisphere.

In summary, there are several methods available to compute ocean advective heat flux. Resolution varies depending upon the method of choice. These measurement techniques fall into two distinct classes, the direct and indirect. The direct method is best suited for small scale, high resolution studies. The indirect method is most useful in large scale climatological studies. Direct methods are accurate but expensive. Indirect methods are more economical but have poor temporal resolution and built in bias.

Comparison of ocean heat flux values computed by these methods shows wide variability, especially in lower latitudes. How can this variability be reduced? Is there a method that would allow for good spatial and temporal resolution without being prohibitively expensive? Tomography may provide the answer to these questions.

2. Tomography Overview

Prior to detailing tomographic measurement of ocean heat flux, it is

appropriate to describe some tomography basics. An excellent review of ocean acoustic tomography is given in Spindel (1985).

a. Travel Time

Eigenrays define fixed acoustic pathways between source and receiver. A sound impulse generated at a source travels simultaneously along many different eigenpaths to the receiver. Since each path has a different length and travels through a different part of the ocean, each eigenray will have a distinct and predictable arrival time associated with it. The arrival times of this multipath signal are represented in Figure 1-3 for the eigenrays given in Figure 1-4.

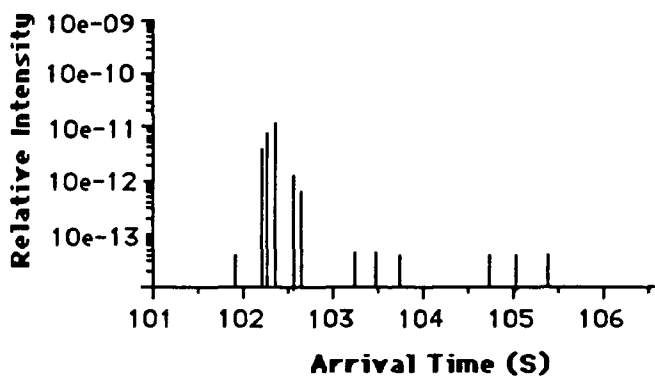


Figure 1-3 Signal Time Series: Time series of a multipath arrival sequence based on the raytrace below.

As the sound pulses travel they "feel" the environment and are perturbed slightly in time by density inhomogeneities and by current along the ray path. By measuring the difference between actual arrival time and the arrival time predicted for the medium in an unperturbed state, one can infer the sound

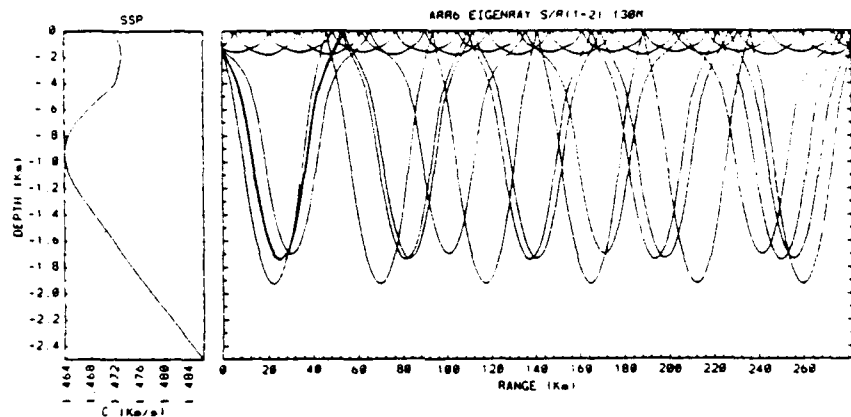


Figure 1-4 Raytrace: Eigenray trace showing typical multipath pattern from the January sound speed profile for the Norwegian Sea region from source 1 to receiver 2.

speed perturbation field along the path. This is known as density tomography .

Ocean currents can be inferred by making simultaneous reciprocal transmissions between a transceiver pair and examining the difference in time of flight along the same eigenpath. Rays traveling with the current will quicken while rays traveling opposed to the current will be delayed. This time difference is proportional to the the current along the ray path.

Inverse techniques can be used to reconstruct the four dimensional sound speed perturbation and the current field from measured travel time series. Further details on inverse theory can be found in a paper by Parker (1977).

b. Tomographic Estimate of Heat Flux

The inversion gives us estimates of the sound speed perturbation field and the zonal and meridional components of current. What remains is to derive potential temperature estimates so that we can proceed with our estimate of heat flux. We do this by assuming that sound speed perturbations are proportional to temperature perturbations. This is a valid assumption provided that salinity does not vary significantly. We then relate perturbations in sound speed to temperature perturbations via the empirical relation giving by Mackenzie (1981). Next we take the perturbations in temperature and form potential temperature perturbations based on empirical relations given in Unesco (1983).

Once potential temperature and the components of current are found, then it is an easy task to compute point estimates of heat flux. These point estimates can then be summed horizontally and vertically to yield integrated flux estimates.

3. Environment

The Norwegian Sea has a number of characteristics that make it a challenging location to study heat flux. The waters are complex and diverse both physically and dynamically. The poleward flow of warm saline North Atlantic water that flows along the Norwegian coast is a sharp contrast to the cooler, less saline waters of the Arctic Basin. In this environment, meanders, jets rings and gyres are not uncommon. Additionally, the ocean's temperature is also quite variable. Sharp thermal gradients are formed at the confluence of the different water masses. These features will provide a good test of the tomographic method. The location of the region where our numerical experiment is conducted is shown in Figure 1-5.

The environment plays a major role in the way heat is transported in the Arctic basin, and it also critically affects acoustic propagation in the region. Seasonal changes modify the water mass structure and directly influence acoustic propagation creating two quite diverse regimes. Bathymetric features

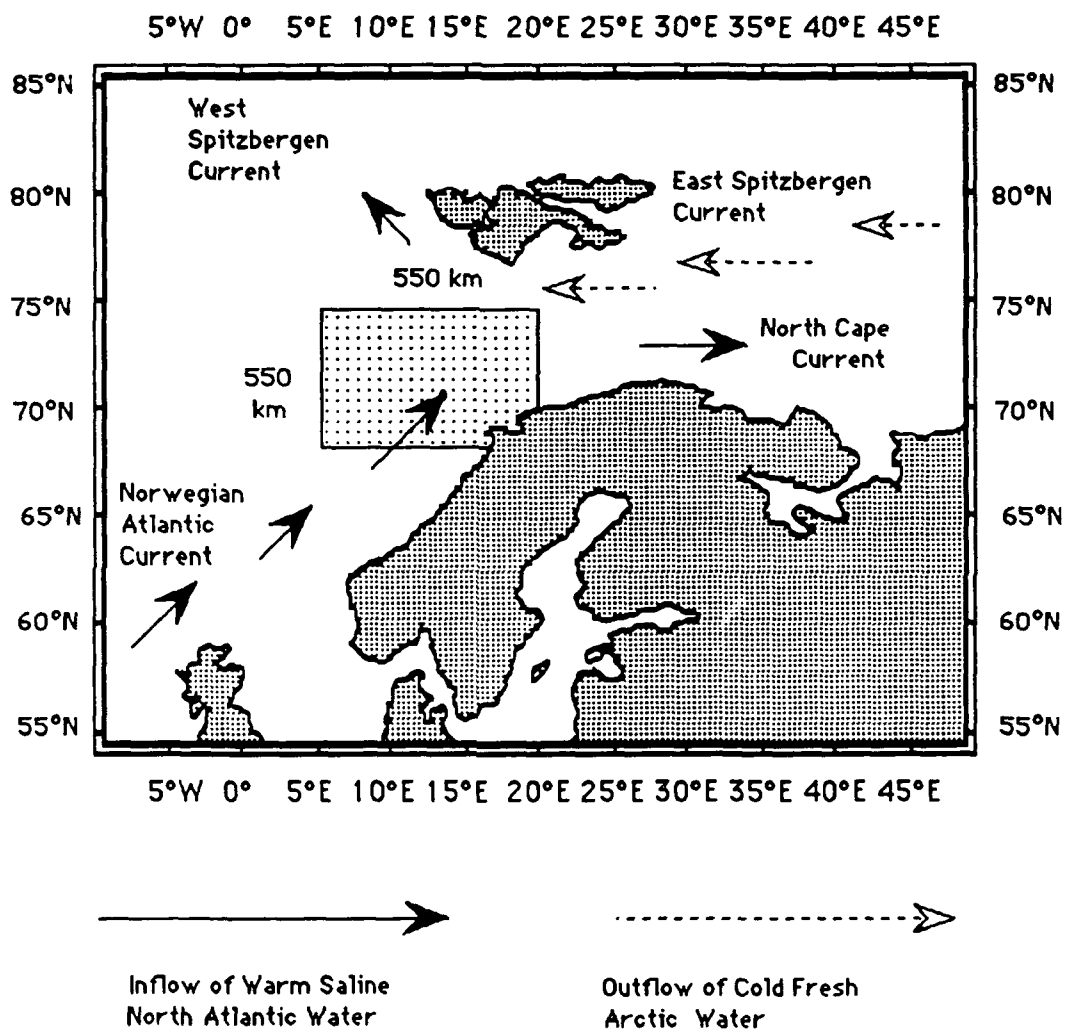


Figure 1-5 Simulation Location: Location of the Tomographic Array for the measurement of Heat Flux.

Seasonal ice formation and breakup processes add complexity to the heat budget such as the shelf break have a controlling influence on the mean flows and the acoustics of the region. Fronts are created at the boundaries of dissimilar water masses. Each of these factors will have an impact on the deployment of a tomographic system.

a. Dominant Flow

The Norwegian Atlantic Current and the Norwegian Coastal Current constitute the dominant flows in the region. Both of these currents are northeasterly, hugging the Norwegian coastline. The Norwegian Atlantic Current is an extension of the Gulf Stream that makes its way through the Faeroe-Shetland Channel importing relatively warm saline water from the North Atlantic. The temperature of this water drops from 8° to 3° Celsius in the winter and 10° to 6° Celsius in the summer by the time it reaches the Spitsbergen area. The Norwegian Atlantic Current is roughly 80 km wide, 500 m deep, flows at 20-40 cm sec⁻¹ and is responsible for a transport of approximately 2-3 Sv. This current is extensively reviewed by Saelen (1962).

The Norwegian Coastal current consists of a wedge of slightly less saline water representing effluent from the Baltic and runoff from the myriad of fiords that are scattered along the Norwegian coast. Flow of the Norwegian Coastal current is considerably less, and has been neglected in previous heat budget calculations.

b. Bathymetry

These flows are heavily influenced by the bathymetry of the region, details of which are described in Hurdle (1986). As the Norwegian Atlantic Current flows north it traces a path directly above the sharply sloping shelf break

where it becomes the northerly flowing branch of the West Spitsbergen Current. The West Spitsbergen Current seems to elude topographic influence from time to time and has been observed to branch into westerly and southerly flows. The easterly flowing North Cape Current is the exception crossing the shelf break and flowing into the shallow Barents Sea basin.

Although under the influence of bathymetry, the Norwegian Atlantic Current is by no means a rigid flow. This current can meander and spin off mesoscale eddies. These features can be advected northward and play a role in the melting of the ice sheets in the marginal ice zone. A description of these eddies created by this flow is given in Saelen (1963).

c. Fronts

Fronts can be expected to exist at the confluence of different water masses and these features complicate sound propagation. Fronts vary in strength and thus their acoustic effect. In this region, they are permanent features that vary in intensity on a seasonal basis with maximum strength in winter. Two fronts lie in close proximity to this study. The Polar Ocean Front is the strongest extending from Spitsbergen southward to Bear Island where the gradient is most intense at 3-4° Celsius per 15 km. The front then turns eastward into the Barents Sea and forms a line of demarcation between the icebound regions to the north and the ice free waters to the south. A weaker extension of the Polar Ocean Front branches westward from Bear Island into the Norwegian Sea. Acoustic paths can be quite variable across fronts making raypath identification difficult.

d. Ice

Ice is a physical barrier that can alter the acoustic path and the travel time and thus has an impact on tomographic system performance. Two

different regimes are apparent. The first involves sheet ice which alters the acoustic reflection characteristics at the surface boundary and the second is free floating ice that may temporarily affect the acoustic path.

The advance of sheet ice in the Barents and Norwegian Sea is mediated by the flow of warm water brought northward by the Norwegian Atlantic Current. The confluence of warm and cold water in the region forms a frontal boundary called the Polar Ocean Front which marks the southern boundary of the ice in this region. We have located the tomographic array well south of this front, thus avoiding the effects of sheet ice altogether.

Concern over free floating ice is minimal due to the northerly flow of warm saline North Atlantic water along the Norwegian coast. Should large ice flows be carried out of the Barents by the East Spitzbergen current, a potential disruption in acoustic paths could occur. These cases would degrade system performance if acoustic pathways were obstructed however, the effect would only be transient in nature and disappear as the ice is advected away.

e. Acoustic Properties

Seasonal changes in the region bring about quite remarkable changes in acoustic propagation in the region. The mean background sound speed profiles are shown in Figure 1-6 for the two monthly climatologies selected for study.

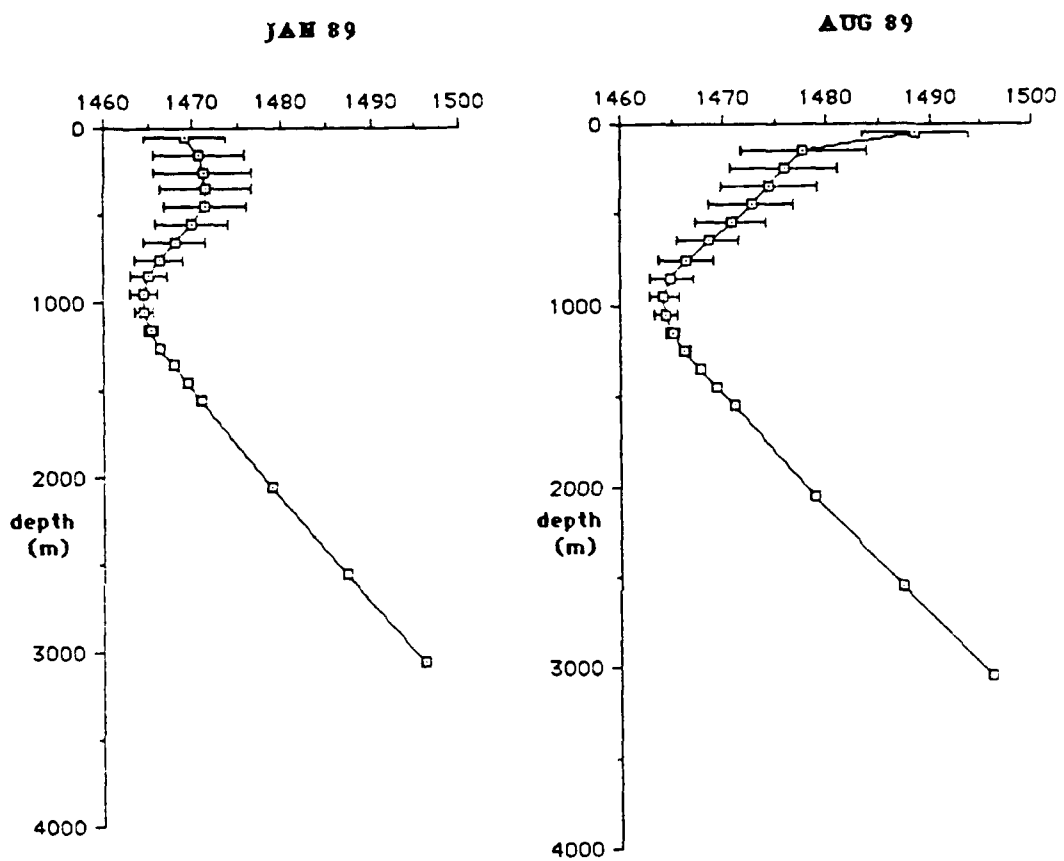


Figure 1-6 Acoustic Environment: Plot of Background Sound Velocity Profiles for January and August 1989. Error bars represent one standard deviation.

Both climatologies show almost identical deep sound channels located at approximately 1000 meters. The near surface profile are very different however. The January 1989 profile shows a local sound speed maximum at roughly 400 meters which establishes a surface duct. This ducting is created by the cooler surface waters that characterize the winter months. The August 1989 profile in contrast shows a decreasing sound speed profile from the surface to the deep sound channel axis, creating a very strong channeling environment in the first kilometer. This channeling environment is a result of the warmer surface waters that characterize the summer months. These two contrasting acoustic regimes will dictate the depth of the array transceiver and the type of eigenrays available for use in this study.

f. Summary

In summary, the environment is expected to have an important impact on tomographic system performance, and does present some serious system complications. Most of these effects are difficult to model and are treated as limitations to scope in this initial study.

II. PHYSICS OVERVIEW

In this chapter we present an overview of the “forward problem” associated with density and current tomography. The “forward problem” specifies the relationship between the observables, (i.e. travel times), and the unknown sound speed perturbation and current fields, we are estimating. We examine the use of a stochastic inverse method that allows us to form estimates of these unknown fields from the observed data. In addition, we discuss statistical measures of system performance. These measures include resolution length and variance. A derivation of heat flux from current and sound speed estimates is also included.

A. TOMOGRAPHIC FORWARD MODELING

1. Time of Flight

In our acoustic model, we require an accurate representation of the path that a sound wave front takes as it travels through the ocean. The path is important because by predetermining the path we can calculate expected travel time of the signals between transceivers in an array. A convenient approach is to model sound propagation using ray theory. We employ ray theory for two basic reasons. Aside from its simplicity, the ray approach offers a good physical representation of the multipath propagation of sound in an acoustic duct. The theory breaks down near caustics and at turning points, consequently corrections must be made. These limitations are not significant enough to lessen the usefulness of this approach. The time of flight of a sound pulse along a given eigenray connecting a source and receiver can be evaluated as follows:

$$T_i + \delta T_i = \int_{\text{path}_i} \frac{ds}{c_0 + \delta c + \vec{V} \cdot \hat{s}} \quad (2.1)$$

a. Density Tomography

Equation (2.1) reveals that the time of flight along any given raypath is inversely proportional to the sound speed and current integrated along the ray path. Upon linearization, the change in travel time resulting from the presence of sound speed perturbations and the flow field along the path and can be expressed as

$$\delta T_i = - \int_{\text{path}_i} \frac{\delta c + \vec{V} \cdot \hat{s} ds}{c_0^2} \quad (2.2)$$

Since $|\delta c| \gg |\vec{V} \cdot \hat{s}|$ we can approximate Equation (2.2) by

$$\delta T_i = - \int_{\text{path}_i} \frac{\delta c ds}{c_0^2} \quad (2.3)$$

It can be seen that travel time perturbation is proportional to the sound speed perturbation summed along the ray path.

b. Current Tomography

Current is related to the difference between travel times along reciprocal paths. A subtraction of reciprocal travel times yield

$$\delta T_i = \int_{\text{path}_i} \left(\frac{1}{C_0 + \delta c + \vec{V} \cdot \hat{S}} - \frac{1}{C_0 + \delta c - \vec{V} \cdot \hat{S}} \right) ds \quad (2.4)$$

upon linearization we get

$$\delta T_i = -2 \int_{\text{path}_i} \frac{\vec{V} \cdot \hat{S} ds}{C_0^2} \quad (2.5)$$

2. Experimental Noise

The forward model is not complete without inclusion of experimental noise. Travel time measurements are contaminated by noise that contains two components, namely measurement noise and model error. Measurement noise results from the lateral displacement of the transceiver element caused by internal waves or tidal effects. Model noise is due to the limits on numerical accuracy and the assumptions that led to the linearization, and discretization of the forward problem. In practice the effects of measurement noise can be circumvented by correcting for transceiver motion or employing various signal processing techniques. A technique that is commonly used is to average the travel time measurements over several transmission cycles. These techniques, as

well as others, are discussed in Spindel (1985). We represent these effects by using a random noise generator to add a noise component to our travel time data.

B. A DISCRETE STOCHASTIC INVERSE METHOD

1. Discretization of an Ocean Volume

In our solution to the inverse problem, we have chosen to discretize the simulated ocean region by dividing it into 605 equal volume boxes measuring 50 x 50 x 0.2 km each. Within each box the sound speed perturbation and current are assumed to be constant. This discretization results in a total of 11 x 11 squares in the horizontal and 5 layers in the vertical. This allows us to cast the continuous integrals in (2.3) and (2.5) as discrete sums. Placing all the data in column vectors, we can re-express the forward problem in matrix-vector form as

$$\delta \underline{T} = \underline{A} \delta \underline{c} + \underline{\epsilon} \quad (2.6)$$

$$\delta \underline{T}' = \underline{B} \underline{V} + \underline{\epsilon}' \quad (2.7)$$

where $\delta \underline{c}$ and \underline{V} are vector parameterizations of the sound speed and current fields respectively. \underline{A} and \underline{B} are linear operators that act as transfer functions relating the unknowns to the data. The vectors $\underline{\epsilon}$ and $\underline{\epsilon}'$ represent the experimental noise. We assume that these errors are uncorrelated with the signal and have a known variance and a zero mean.

2. Gauss-Markoff Estimate

Equations (2.6) and (2.7) represent a highly underdetermined system, that is there are many more unknowns than equations or data. There is infinite number of solutions satisfying these equations. The best solution however, should fit the data as well as the statistical a priori information. A useful method that

requires the optimal solution to have minimum mean square error is given by the Gauss-Markoff theorem. This method states that the optimal estimate can be evaluated, assuming $\hat{\delta}_{\underline{C}}$ and $\hat{\underline{V}}$ are uncorrelated, as

$$\hat{\delta}_{\underline{C}} = \underline{C}_{\underline{e}} \underline{A}^T \underline{C}_{\underline{e}}^{-1} \hat{\delta}_{\underline{T}} \quad (2.8)$$

$$\hat{\underline{V}} = \underline{C}_{\underline{v}} \underline{B}^T \underline{C}_{\underline{e}'}^{-1} \hat{\delta}_{\underline{T}} \quad (2.9)$$

where

$$\underline{C}_{\underline{e}} = \underline{C}_{d\underline{e}} - (\underline{C}_{d\underline{e}} \underline{A}^T)(\underline{A} \underline{C}_{d\underline{e}} \underline{A}^T + \underline{C}_{\underline{e}})^{-1} (\underline{C}_{d\underline{e}} \underline{A}^T)^T \quad (2.10)$$

$$\underline{C}_{\underline{h}} = \underline{C}_{\underline{v}} - (\underline{C}_{\underline{v}} \underline{B}^T)(\underline{B} \underline{C}_{\underline{v}} \underline{B}^T + \underline{C}_{\underline{e}'})^{-1} (\underline{C}_{\underline{v}} \underline{B}^T)^T \quad (2.11)$$

are the error covariances of $\hat{\delta}_{\underline{C}}$ and $\hat{\underline{V}}$ respectively, and $\underline{C}_{\underline{e}}$ and $\underline{C}_{\underline{e}'}$ are the covariance matrices of experimental noise \underline{e} and \underline{e}' respectively. An appealing property of the Gauss-Markoff estimator is that it does not require the shape of the probability density functions of the unknowns.

3. Covariance Functions

In order to reconstruct the sound speed perturbation field and current field using the Gauss-Markoff method we need to specify the covariances of the fields. It is through the covariance matrices that we are able to specify "a priori knowledge" concerning the unknowns. In the inversion of the data, we assume that the sound speed perturbation field and the zonal and meridional current field are uncorrelated with each other. Furthermore we assume that all these fields are

statistically homogeneous and their correlation functions have gaussian shapes, that is

$$\text{Cov}_{\delta c}(\Delta x, \Delta y, \Delta z) = \sigma_{\delta c}^2 \exp^{-\left[\left(\frac{\Delta x}{L_x} \right)^2 + \left(\frac{\Delta y}{L_y} \right)^2 + \left(\frac{\Delta z}{L_z} \right)^2 \right]} \quad (2.12)$$

$$\text{Cov}_{v_x}(\Delta x, \Delta y, \Delta z) = \sigma_{v_x}^2 \exp^{-\left[\left(\frac{\Delta x}{L_x} \right)^2 + \left(\frac{\Delta y}{L_y} \right)^2 + \left(\frac{\Delta z}{L_z} \right)^2 \right]} \quad (2.13)$$

$$\text{Cov}_{v_y}(\Delta x, \Delta y, \Delta z) = \sigma_{v_y}^2 \exp^{-\left[\left(\frac{\Delta x}{L_x} \right)^2 + \left(\frac{\Delta y}{L_y} \right)^2 + \left(\frac{\Delta z}{L_z} \right)^2 \right]} \quad (2.14)$$

The covariance function is inexact, but a good approximation if the correlation lengths L_x , L_y , and L_z approach the true correlation lengths of the ocean environment. that correspond to the true ocean environment. The $\Delta x, \Delta y, \Delta z$ values represent the separation between two points in the given direction. The quantities $\sigma_{\delta c}$, σ_{v_x} and σ_{v_y} are the rms values of the respective unknowns. Values for $\sigma_{\delta c}$ are roughly 5 meters sec⁻¹ while σ_v values are around 0.5 meters sec⁻¹. The larger the correlation length, the more information we specify to the estimator. In the inversions we used horizontal lengths of 50-100 km and vertical length of .2-.6 km. These values lie at the upper limit of size for mesoscale features in the region.

4. Error

Error in the estimate, denoted by subscripts ξ and η in Equations (2.8) and (2.9), can be broken down into two statistically independent components. These components are the bias,

$$b = \langle \hat{\delta}_{\underline{c}} \rangle - \delta_{\underline{c}} \quad (2.15)$$

$$d = \langle \hat{V} \rangle - V \quad (2.16)$$

and random error

$$\Delta(\hat{\delta}_{\underline{c}}) = \hat{\delta}_{\underline{c}} - \langle \hat{\delta}_{\underline{c}} \rangle \quad (2.17)$$

$$\Delta \hat{V} = \hat{V} - \langle \hat{V} \rangle \quad (2.18)$$

where $\langle \hat{\delta}_{\underline{c}} \rangle$ and $\langle \hat{V} \rangle$ are the expected value of $\hat{\delta}_{\underline{c}}$ and \hat{V} respectively.

Bias is attributed to systematic error, which is a function of sample size. As the size of the sample data increases, bias is expected to decrease and vice versa. Random error results from the randomness of the data itself, which contains measurement error and model error. The total mean square error is

$$C_{\varepsilon} = C_{\Delta \hat{\delta}_{\underline{c}}} + \langle bb^T \rangle \quad (2.19)$$

$$C_{\eta} = C_{\Delta \hat{V}} + \langle dd^T \rangle \quad (2.20)$$

The covariances of the randomness are:

$$C_{\Delta \hat{\delta}_{\underline{c}}} = C_{\varepsilon} A^T C_e^{-1} A C_{\varepsilon} \quad (2.21)$$

$$C_{\Delta \hat{V}} = C_{\eta} B^T C_e^{-1} B C_{\eta} \quad (2.22)$$

5. Resolution

Having derived the statistical measures of error we now derive measures of system resolution. The following discussion of system resolution starts with an application of a singular value decomposition as described by Chiu (1987). The operators in Equation (2.21) and (2.22) can be decomposed as

$$[C_e^{-1/2} A \ C_{\delta_e}^{1/2}] = U \Lambda V^T \quad (2.23)$$

$$[C_e^{-1/2} B \ C_v^{1/2}] = Q P S^T \quad (2.24)$$

where the diagonal elements λ_i of matrix Λ and ϕ_i of matrix P are the associated singular values, and the columns u_i, v_i and q_i, s_i of the matrices U, V and Q, S represent the left and right singular vectors defining the parameter and data spaces.

Following the derivation given by Chiu *et al* (1987), the minimum mean square error estimate can be expressed in terms of the singular vectors as

$$C_{\delta_e}^{-1/2} \delta_e^\wedge = \sum_{i=1}^k \frac{\lambda_i}{\lambda_i^2 + 1} [u_i^T C_e^{-1/2} \delta T] v_i \quad (2.25)$$

and

$$C_v^{-1/2} \hat{V} = \sum_{i=1}^k \frac{\Phi_i}{\Phi_i^2 + 1} [q_i^T C_e^{-1/2} \delta T] s_i \quad (2.26)$$

The solution for each estimate is obtained by taking a weighted sum of the base vectors \underline{V}_i and \underline{S}_i . The diagonal elements λ_i and ϕ_i are analogous to signal to noise ratios. For example, when λ_i^2 or $\phi_i^2 \gg 1$, the signal dominates, and in the opposite case, noise dominates. The linear optimal estimator acts to downweight the noise while passing the signal.

Following the discussion of Chiu (1987), we define a symmetric matrix R as the resolution matrix such that

$$R_{\delta c} = V \Lambda (I - \Lambda^2)^{-1} \Lambda V^T \quad (2.27)$$

$$R_{\underline{V}} = S P (I - P^2)^{-1} P S^T \quad (2.28)$$

The rows and columns in this matrix correspond to the resolution kernel, which represents the best estimate of a delta function. Substituting the resolution matrix into Equations (2.27) and (2.28) and performing some manipulation, we come up with

$$C_{\epsilon} = C_{\delta c}^{1/2} (I - R_{\delta c}) C_{\delta c}^{1/2} \quad (2.29)$$

$$C_{\underline{V}} = C_V^{1/2} (I - R_V) C_V^{1/2} \quad (2.30)$$

These Equations shows that for the minimum mean square error estimate, the relationship between error and resolution is linear. As resolution

increases, error decreases and vice-versa. When $R = I$, $C\varepsilon = 0$, the ideal resolution situation exists.

As a means of describing the system resolution, we adopt Chiu's (1987) measure of horizontal and vertical resolution length H and V respectively. For each unknown field, i.e. sound speed perturbation or current, these quantities represent the horizontal and vertical distances for which approximately 70% ($\pm 1 \sigma$) of the total energy of the resolution kernel associated with a given location is confined. The minimum resolution lengths in the three spatial coordinates is calculated by

$$H_x(ix, iy, iz) = 2 \sqrt{\sum_{jx}^{nx} \sum_{jy}^{ny} \sum_{jz}^{nz} [(jx - ix)dx]^2 r_i^2(jx, jy, jz) E_i^{-1}} \quad (2.31)$$

$$H_y(ix, iy, iz) = 2 \sqrt{\sum_{jx}^{nx} \sum_{jy}^{ny} \sum_{jz}^{nz} [(jy - iy)dy]^2 r_i^2(jx, jy, jz) E_i^{-1}} \quad (2.32)$$

$$V(ix, iy, iz) = 2 \sqrt{\sum_{jx}^{nx} \sum_{jy}^{ny} \sum_{jz}^{nz} [(jz - iz)dz]^2 r_i^2(jx, jy, jz) E_i^{-1}} \quad (2.33)$$

where

$$E_i^{-1} = \sum_{jx}^{nx} \sum_{jy}^{ny} \sum_{jz}^{nz} r_i^2(jx, jy, jz) \quad (2.34)$$

where j_x, j_y, j_z are three dimensional box indices and \mathbf{L}_i^2 is the resolution kernel.

H_x, H_y and V represent the minimum resolution length in each spatial coordinate. An important point to note is that RMS error and resolution length do not depend on the environmental data δT , but rather on the sound speed perturbation covariance matrix $C_{\delta c}$ or the covariance matrix of the current C_V and the array geometry.

6. Heat flux estimate and error

We can estimate sensible temperature from the sound speed field by using an empirical relation given in Mackenzie (1983). Sensible temperature can be related to potential temperature by an empirical relation given in UNESCO (1981). We use these relationships to compute the potential temperature from the sound speed field throughout the model. Heat flux estimates can be constructed from $\hat{\theta}$ and \hat{V} as follows

$$\hat{F}_x = \rho C_p \hat{\theta} \hat{V}_x \quad (2.35)$$

$$\hat{F}_y = \rho C_p \hat{\theta} \hat{V}_y \quad (2.36)$$

where \hat{F}_x, \hat{F}_y and \hat{V}_x, \hat{V}_y are the zonal and meridional components of heat flux and current respectively.

The error in the heat flux estimate is related to the error in the individual parameters. Assuming the individual errors in $\hat{\theta}, \hat{V}_x$, and \hat{V}_y are uncorrelated, we can determine the variance of each estimate by letting

$$e_\theta = \theta - \hat{\theta} \quad (2.37)$$

$$e_{v_x} = V_x - \hat{V}_x \quad (2.38)$$

$$e_{v_y} = V_y - \hat{V}_y \quad (2.39)$$

be the individual errors. The mean square error of each flux estimate is

$$\langle e_{f_x}^2 \rangle = \langle (f_x - \hat{f}_x)^2 \rangle = \rho C_p \langle \theta V_x - \hat{\theta} \hat{V}_x \rangle \quad (2.40)$$

$$\langle e_{f_y}^2 \rangle = \langle (f_y - \hat{f}_y)^2 \rangle = \rho C_p \langle \theta V_y - \hat{\theta} \hat{V}_y \rangle \quad (2.41)$$

Substituting the error represented in (2.37), (2.38), and (2.39) into Equation (2.40) and (2.41) and collecting the lowest order terms we have

$$\langle e_{f_x}^2 \rangle = [\theta^2 \langle e_{V_x}^2 \rangle + V_x^2 \langle e_\theta^2 \rangle] \quad (2.42)$$

$$\langle e_{f_y}^2 \rangle = [\theta^2 \langle e_{V_y}^2 \rangle + V_y^2 \langle e_\theta^2 \rangle] \quad (2.43)$$

Assuming that the errors are small one can replace the actual values θ , V_x , and V_y in (2.42) and (2.43) with the estimates $\hat{\theta}$, \hat{V}_x , and \hat{V}_y .

C. SUMMARY

In summary, we have presented an overview of the forward problem of density and current tomography. We have shown the relationship between the travel time data and the sound speed perturbation and current fields we are estimating. The derivation of the heat flux estimate and its mean square error were presented. We then reviewed the Gauss-Markoff technique which enables

us to invert the data for optimal estimates of the unknown fields. We discuss some useful statistical measures of system performance. These are the horizontal and vertical resolution lengths and mean square error.

III. NUMERICAL OCEAN AND ARRAY SIMULATIONS

A. SYNTHETIC OCEAN

The synthetic ocean represents the "truth" in this numerical experiment. A realistic Norwegian Sea environment is simulated through the use of GDEM climatology.

1. Spatial Resolution

Selection of spatial resolution becomes a tradeoff between computer resources available and the desire to express the fine spatial detail to adequately describe the flow in the region. The simulation experiment was performed on a VAX GPX minicomputer. A reasonable tradeoff between resolution and computation time limited the model domain to a region of $550 \times 550 \times 1 \text{ km}^3$. The model domain was subdivided into 605 equal-volume boxes each measuring $50 \times 50 \times .2 \text{ km}$. This arrangement allows for simulation of a $302,500 \text{ km}^3$ ocean volume at a resolution high enough to include most mesoscale variability in the upper 1 km.

Vertical resolution of the synthetic ocean is an important consideration given the baroclinic nature of the temperature field and the moderate vertical shear seen in the geostrophic current data. The strongest vertical temperature and current gradients are located in the near surface regime. A 200 meter depth increment was chosen to provide the optimal balance between adequately defining the field and keeping the problem tractable on a minicomputer.

2. Bathymetry

Due to the unavailability of precise bathymetry and the uncertainties of modeling absorption and reflection with the bottom in the region, we have restricted our study to only non-bottom interacting rays.

3. GDEM Data Base

The model ocean is derived from GDEM climatology made available by Fleet Numerical Oceanography Center. GDEM is a synthetic data base of temperature and salinity profiles that cover 30 depths irregularly spaced from the surface to 5000 meters. Synthetic profiles of temperature and salinity are based on regression equations built from a data base of over four million observations. GDEM climatologies are available in monthly, seasonal or annual time frames. In this experiment, we choose two mean climatologies for the months of January 89, and August 89, representing annual extremes in temperature. The irregularly spaced GDEM data given in geodetic coordinates were mapped into a regularly spaced Cartesian system in the model domain using cubic splines. The climatological data base contains information only on the average structure of the ocean. Therefore, some mesoscale and sub-mesoscale variability that are present in the real world are not represented in the synthesized ocean.

4. Model Parameters

Once temperature and salinity data were obtained on a regular grid, other model parameters were computed at each grid point. Sound speed was computed using the empirical formula given by Mackenzie (1981) and then separated into a background, $C_0(z)$, and a perturbation field $\delta c(x,y,z)$. Potential temperature was calculated using the empirical formula given in UNESCO (1983) using the GDEM temperature and salinity data. The actual sound speed

perturbation field and potential temperature fields for 5 levels of the model for January and August 1989 are presented in Figures 3-1 and 3-2.

Geostrophic current was also computed using the GDEM temperature and salinity data. The geostrophic approximation is used to derive the velocity field because no current fields were available, in the data base and geostrophy represents a physical way to generate synthetic velocity fields. Figure 3-3 shows the derived current fields for January and August 1989 respectively.

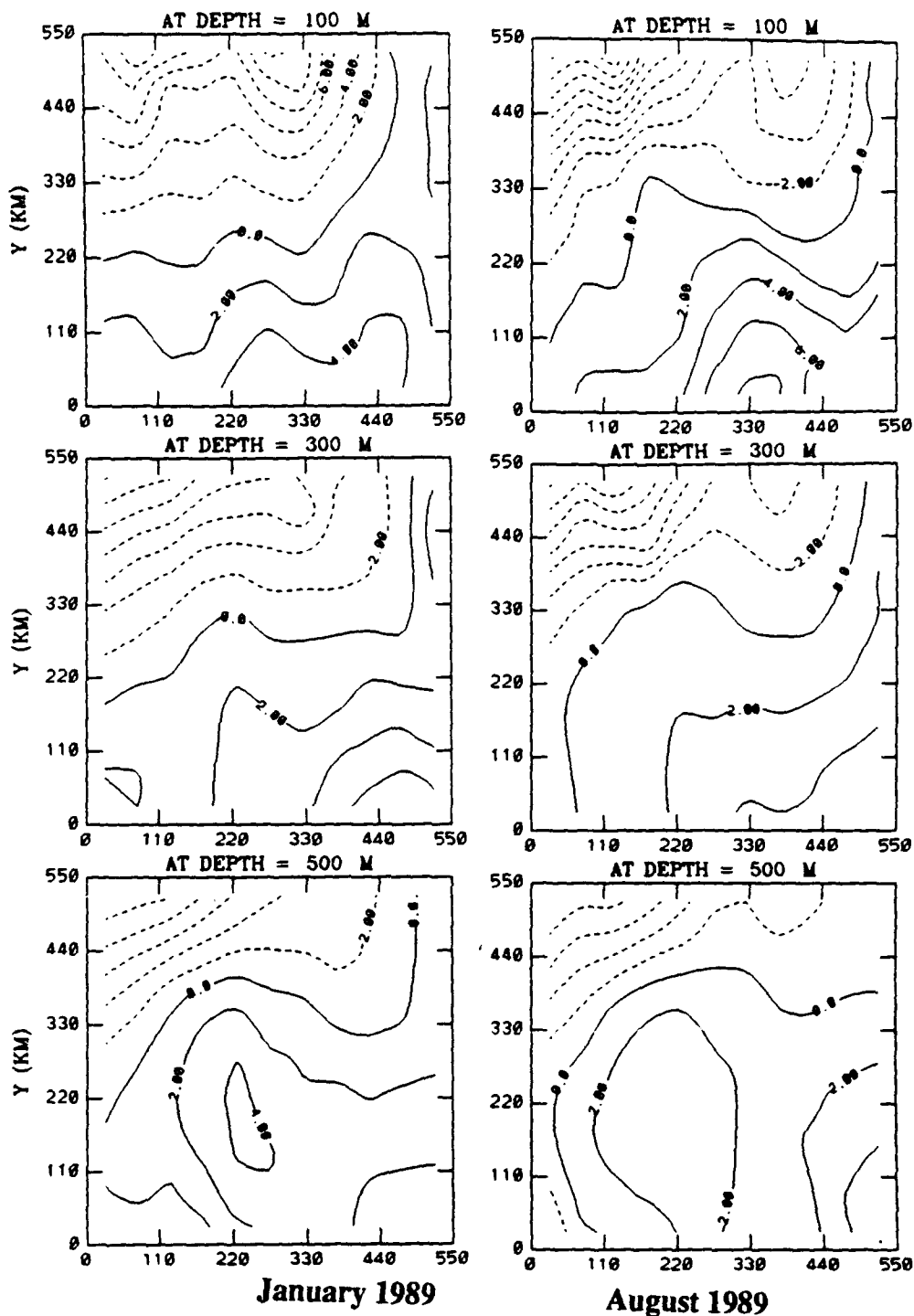
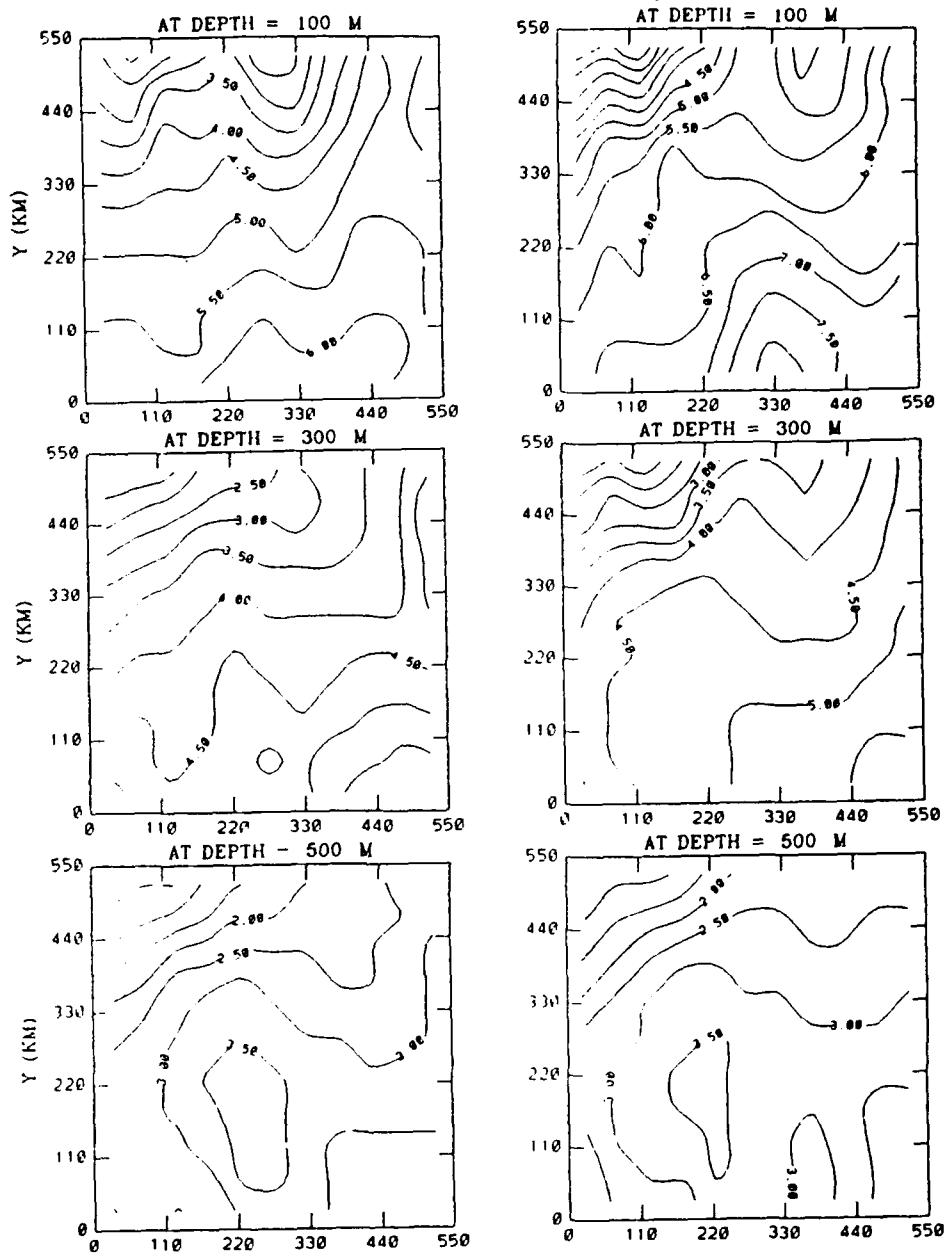


Figure 3-1 Sound Speed Perturbation Field: Contouring of the actual January and August 89 sound speed perturbation fields at three depth levels. Units are in meters sec^{-1}



January 1989

August 1989

Figure 3-2 Temperature Fields: Contouring of the "actual" January and August 89 potential temperature fields in degrees C at three depth levels.

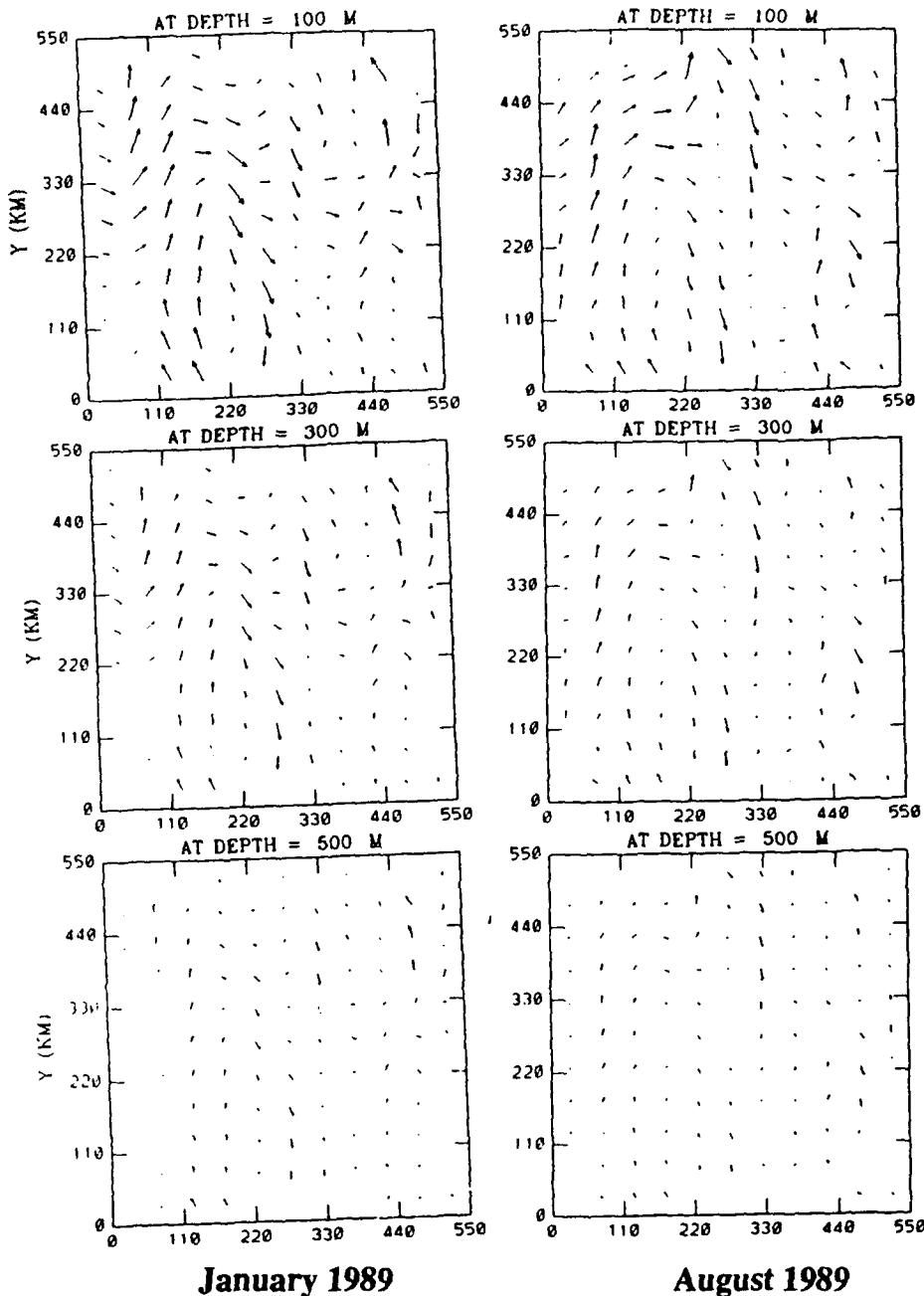


Figure 3-3 Current Fields: The “actual” January and August 89 geostrophic velocity field at three depth levels. The magnitude of the current ranges from $.1\text{-.5}$ meters sec $^{-1}$ at these depths.

5. Acoustic Environment

Both climatologies show a deep sound channel located at approximately 1000 meters (see Figure 1-7). The near surface profiles are very different however. The January 1989 profile shows a sound speed maximum at roughly 400 meters which establishes a surface duct. This ducting is created by the cooler surface waters that characterize the winter months. The August 1989 profile in contrast shows decreasing sound speed from the surface to the deep sound channel axis, creating a channeling environment. This channeling environment is a result of the warmer surface temperatures that characterize the summer months. These two contrasting acoustic regimes will govern the optimal depth of the array sources and receivers and the type of eigenrays available for use.

B. ARRAY GEOMETRY

Two six, element arrays are simulated in this experiment, and they are depicted in Figure 3-4. The large array has been given the name Steven and the small array, Harry. These geometries were selected to answer two basic questions. The first one is, how much area can be covered by a six element array whose purpose is the measurement of heat flux? Another question is how does system resolution vary with array size.

These two array geometries should in principle have advantages under different circumstances. Steven should be better suited to cover a larger area with less resolution, while Harry would be better suited to cover a smaller area at greater resolution . Both geometries are compared in a quantitative sense and many more arrangements are possible.

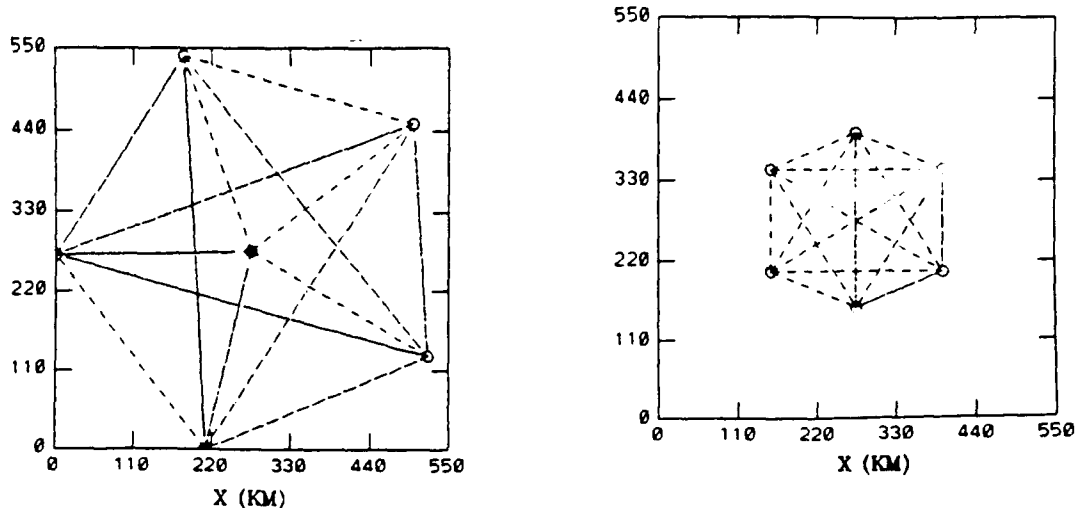


Figure 3-4 Array Geometry: Two 6 element arrays, Steven (large) and Harry (small), simulated in this experiment.

C. RAY TRACING

With the background sound speed profile determined array geometries selected ray tracing can proceed. Eigenrays are calculated using a raytrace algorithm based on a 4th order Runge-Kutta numerical integration technique for selected horizontal configurations and transceiver depths. In this experiment we identified all eigenrays that had a launch angle lying between -15° and $+15^\circ$. Eigenrays having unique trajectories were selected to comprise the data set for inversion. This provided between 3 and 10 eigenrays for each transceiver pair. Sample eigenray traces are shown in Figures (3-5) and (3-6) for January and August 89 climatology.

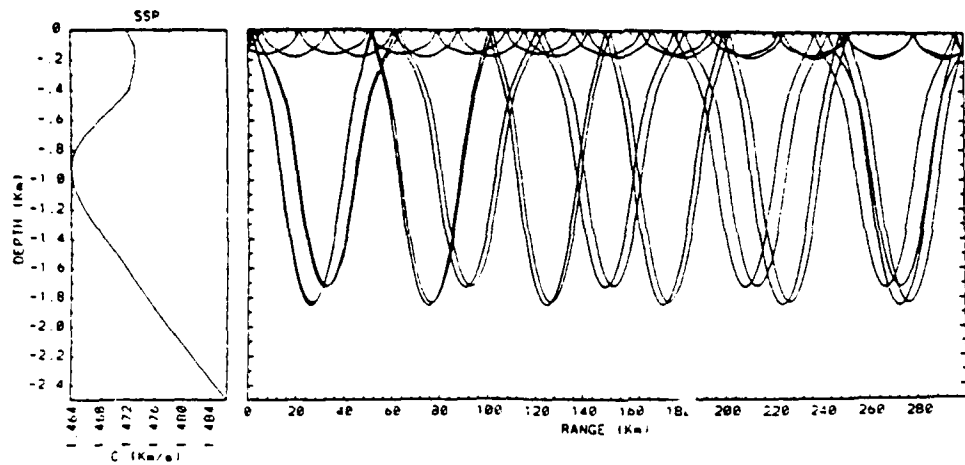


Figure 3-5 Raytrace: Eigenray trace for a transceiver pair from array Steven from January 1989 climatology.

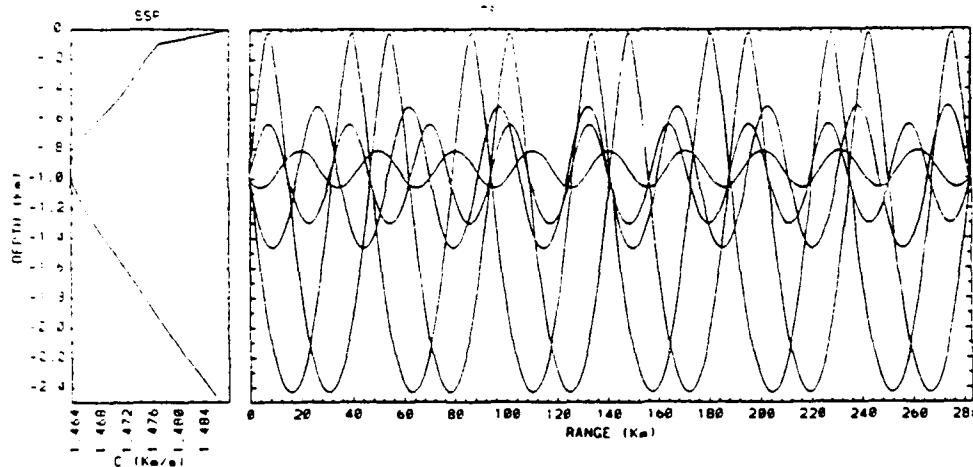


Figure 3-6 Raytrace: Eigenray trace for a transceiver pair from the Steven array from August 1989 climatology.

D. SYNTHETIC TRAVEL TIME DATA

Synthetic travel time data are computed for the two array geometries using the actual sound speed perturbation and current fields. We add to these signals a random error component to simulate experimental noise.

E. INVERSION

Our intention is to assess the tomographic method on its own merits. Thus in our inversion we specify no physical or dynamical constraints. Travel time data are inverted using two specialized software programs, one for density and the other for current. The output of these programs are the estimate of sound speed perturbation and the zonal and meridional components of current. These estimated fields are compared to the actual fields at each level in the model. In addition, the reconstructed perturbation fields are added to the background field to obtain the total sound speed field. Estimates of potential temperature are made using the total sound speed field as previously described. Point estimates of zonal and meridional heat flux are then computed.

F. RESOLUTION

The performance of an array can be assessed using statistical means independent of any data. A system resolution analysis can help to determine the appropriate geometry for heat flux measurement. We can calculate the horizontal and vertical resolution lengths of each array using the method described in the previous chapter.

A desirable array is one which can adequately resolve both the temperature and current fields, and yet can cover as much area as possible. How much area can a six element array cover and still adequately resolve temperature and

current structure in the Norwegian Sea? Which measurement, temperature or current will have the most stringent resolution requirements. for the determination of heat flux Answer these questions are given in a resolution analysis presented in the next chapter.

IV. RESULTS AND DISCUSSION

In this chapter we discuss the results of our investigation. First we show a resolution analysis which quantifies tomographic array performance. Next, we compare the actual error in the estimated fields to the root mean square error predicted by the Gauss-Markoff estimator. A direct comparison of the actual and estimated fields is then followed. We do this for potential temperature, current, and then heat flux. We consider our assessment to be a conservative one since we have used rather inexact a priori information and high noise levels for the monthly estimates.

The two climatologies used in this simulation provide a formidable test of the tomographic system. The temperature fields for each month contain some rather fine horizontal structure. For example, both climatologies contain a warm core eddy feature, that is expressed at 500 meters and below. At depths above 500 meters a frontal feature is present in the North-West quadrant of the model domain. The current field is also complex. There is a anticyclonic gyre superimposed on a warm core feature and rather sharp oscillations are apparent in the both zonal and meridional components of the current field. The meridional component of the current is dominant while the zonal component is weaker. The question of how well these fields can be estimated depends on how well tomography samples the ocean volume.

A. RESOLUTION

1. Sound speed perturbation field

Resolution length defines the smallest feature that can be resolved by an array. Horizontal resolution depends on array geometry. Vertical resolution depends on the characteristics of the acoustic environment. Figure 4-1 through 4-3 show the minimum horizontal and vertical resolution length for the January 89 sound speed perturbation field. These results are summarized in Table 4.1. Horizontal resolution lengths for the sound speed perturbation field averages about 120 km for array Steven while for array Harry it averages 30 km. The improved resolution for the Harry is due to the compact design. Horizontal resolution decreases slightly with depth for both arrays. Harry, by virtue of compactness provides better resolution overall and seems to do slightly better in the meridional direction. Vertical resolution is about the same for both geometries, with a minimum resolution length of 440-480 meters. Vertical resolution depends heavily on the trajectory of the eigenrays .

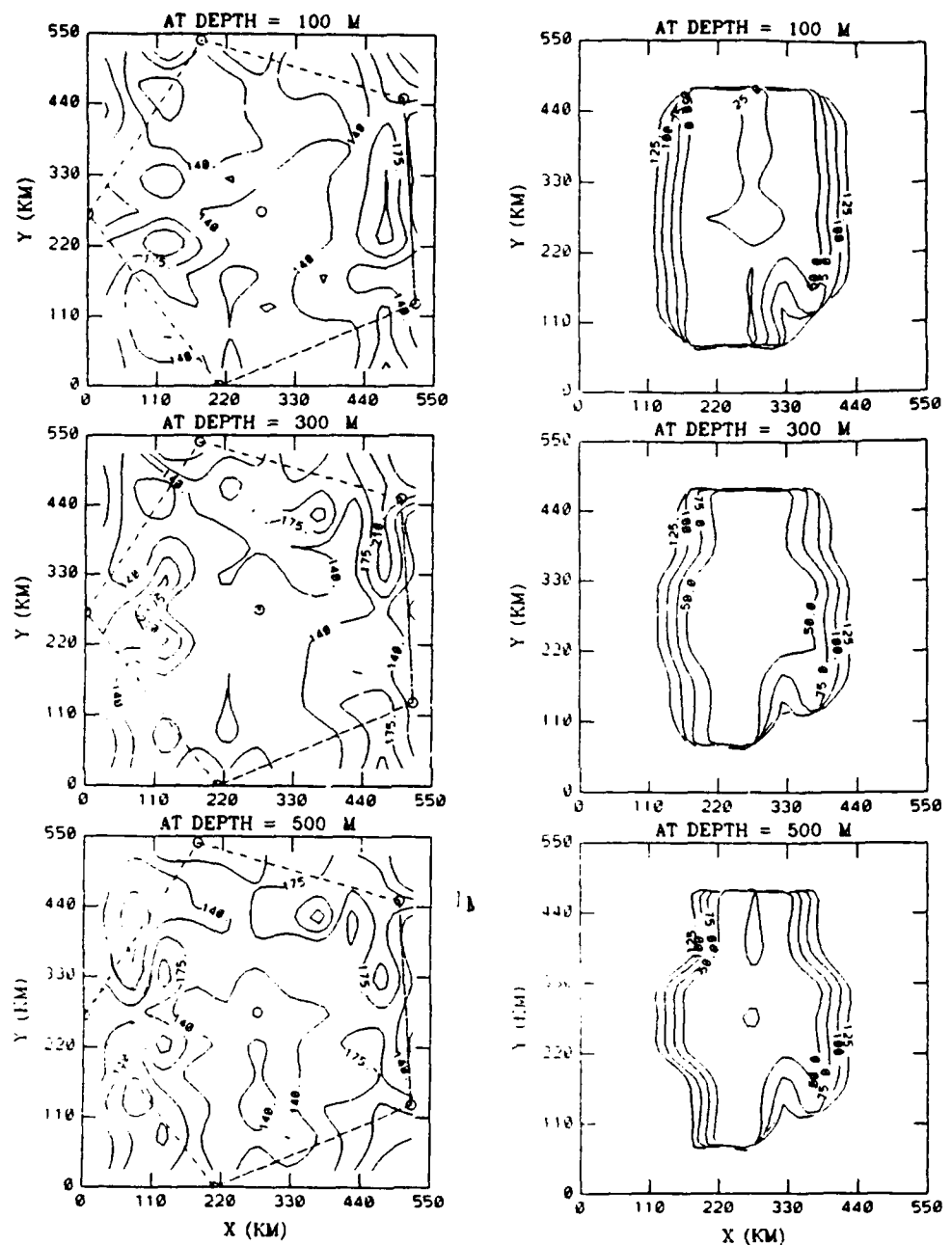
TABLE 4.1 Summary of the resolution analysis of the January δc field.

Resolution Length	Array Steven	Array Harry
Zonal (km)	120	30
Meridional (km)	120	25
Vertical (m)	400	240

A look at horizontal resolution for the August case reveals that the horizontal resolution is about the same; however, vertical resolution is 30-40% poorer. The poorer vertical resolution is due to the channeling nature of the

acoustic environment. A way to improve the vertical resolution of the August case would be to couple tomography with satellite measurement of sea surface temperature (SST). The inclusion of satellite data is suggested as a topic for future study.

In summary the horizontal resolution array Harry is four times better than array Steven for the sound speed perturbation field. The vertical resolution was roughly 15% better for Harry when compared to array Steven. Horizontal resolution length is roughly 20% of the array diameter for array Steven while 12% of array diameter for array Harry.



Array Steven

Array Harry

Figure 4-1 Resolution: Minimum Zonal Resolution length (km) of the January 89 sound speed perturbation field for two array geometries.

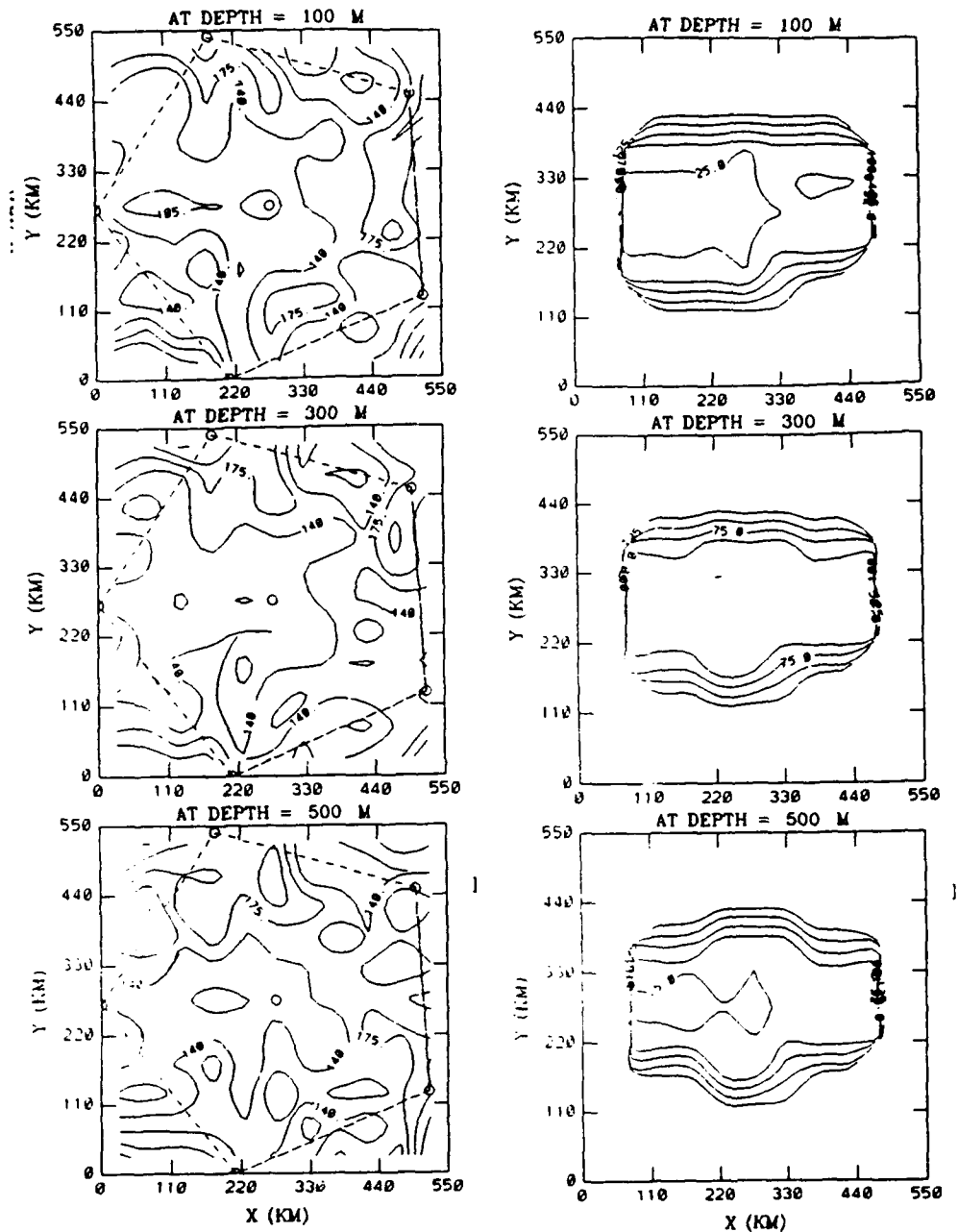
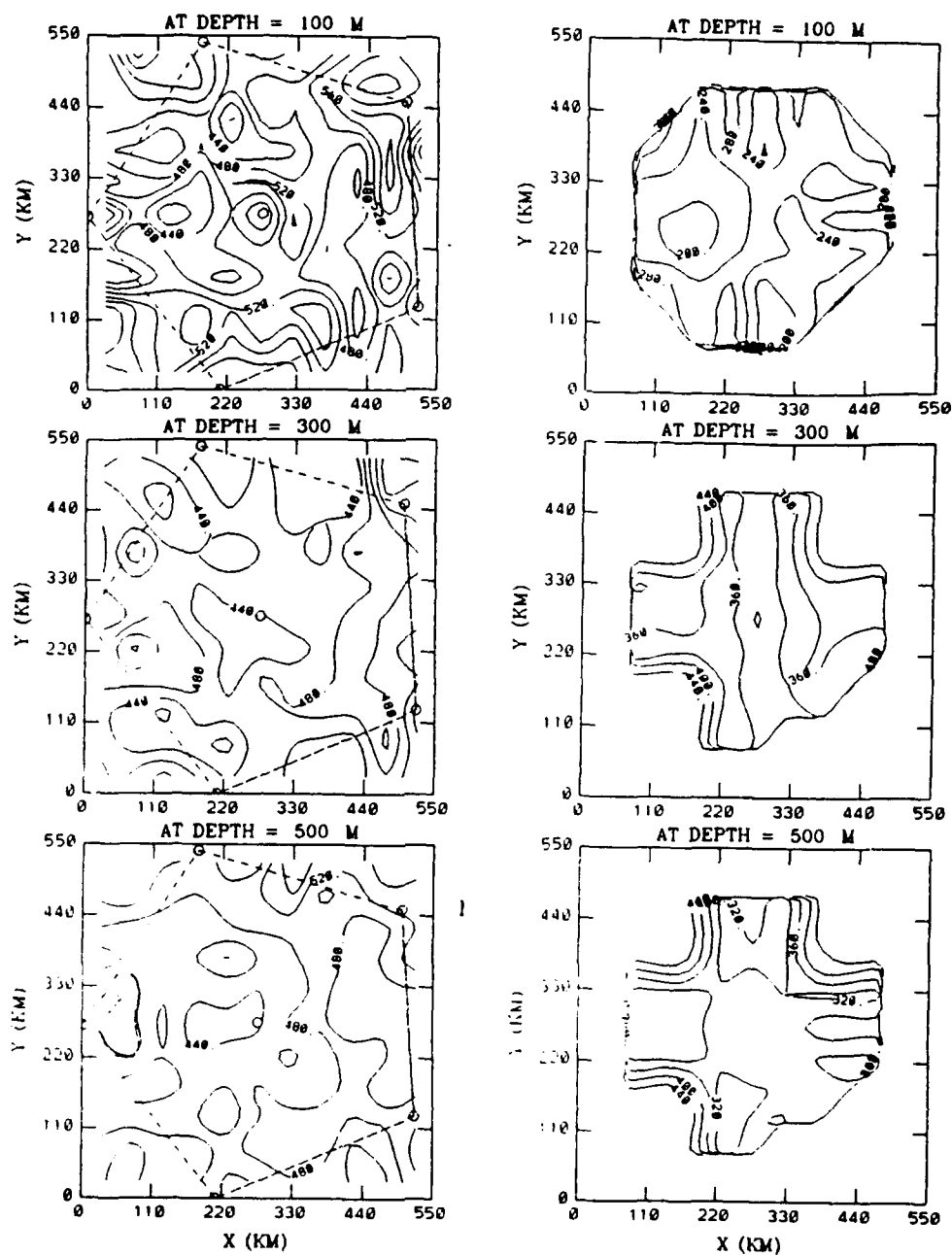


Figure 4-2 Resolution: Minimum meridional resolution length (km) of January 89 sound speed perturbation field for two array geometries.

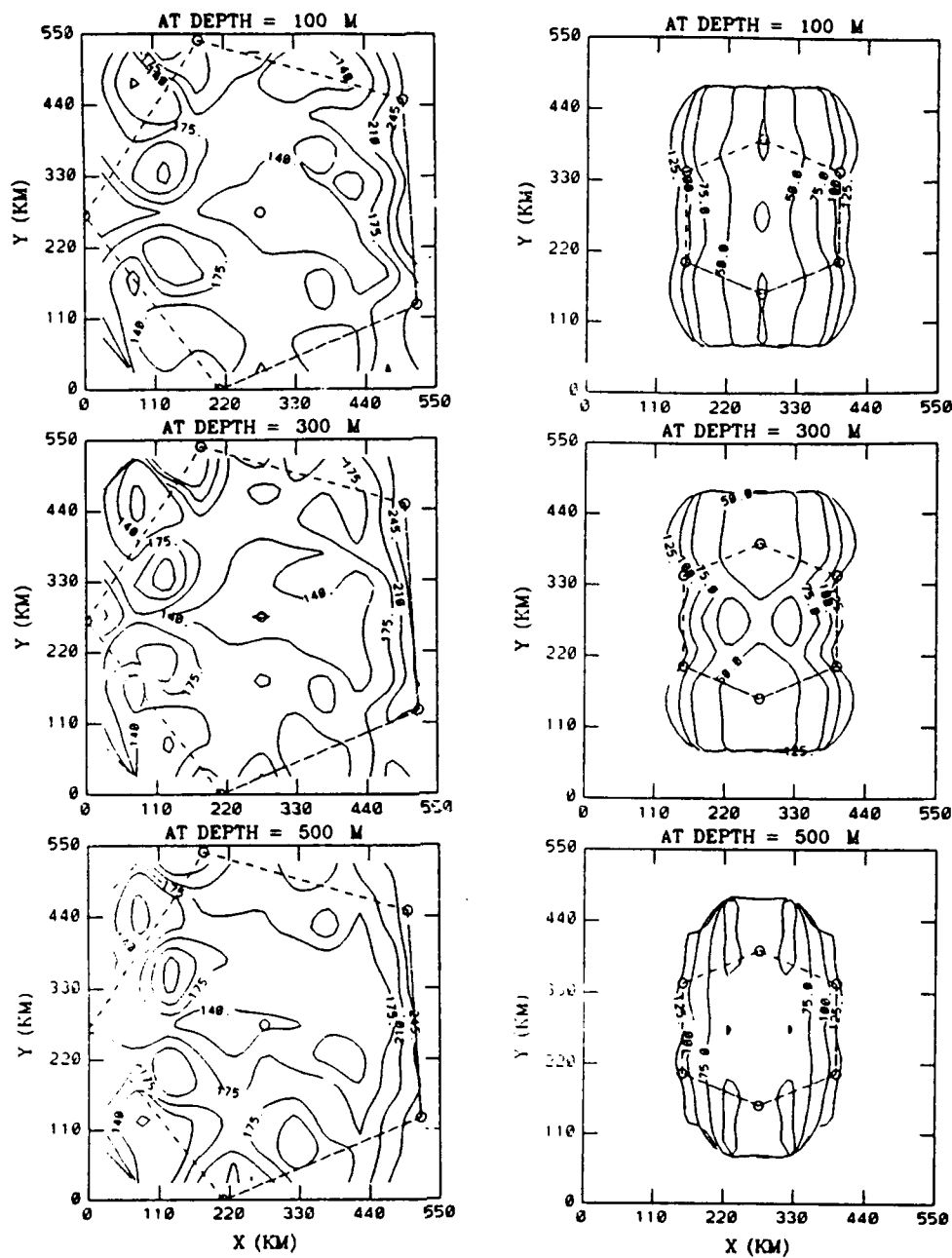


2. Current field

Resolution of the January 89 current field is presented for the two arrays in Figures 4-4 through 4-9. A summary of these results is given in Table 4.2. In comparing the resolution of the zonal component of current for both arrays in the zonal direction, we observe in Figure 4-4 that Harry does significantly better with a resolution length of 35 km. Zonal resolution in the meridional direction is 25 km for Harry and remains at 125 km for Steven as is shown in Figure 4-5.

TABLE 4-2 Summary of Resolution Analysis for current.

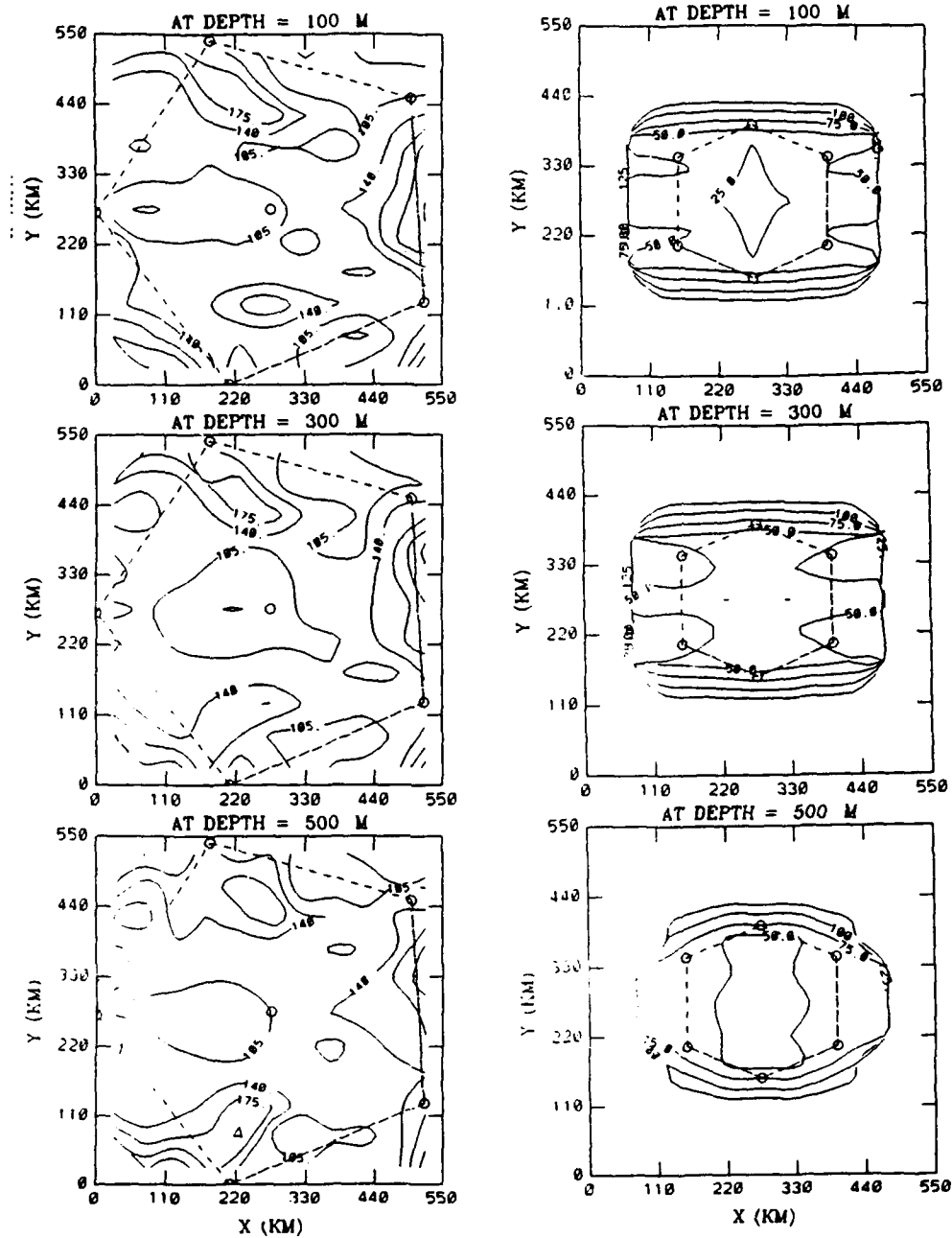
Resolution Length	Array Steven	Array Harry
Zonal Current	125	40
Zonal Direction km		
Zonal Current	125	35
Meridional Direction km		
Zonal Current	400	360
Vertical Direction m		
Meridional Current	125	35
Zonal Direction km		
Meridional Current	125	45
Meridional Direction km		
Meridional Current	440	240
Vertical Direction m		



Array Steven

Array Harry

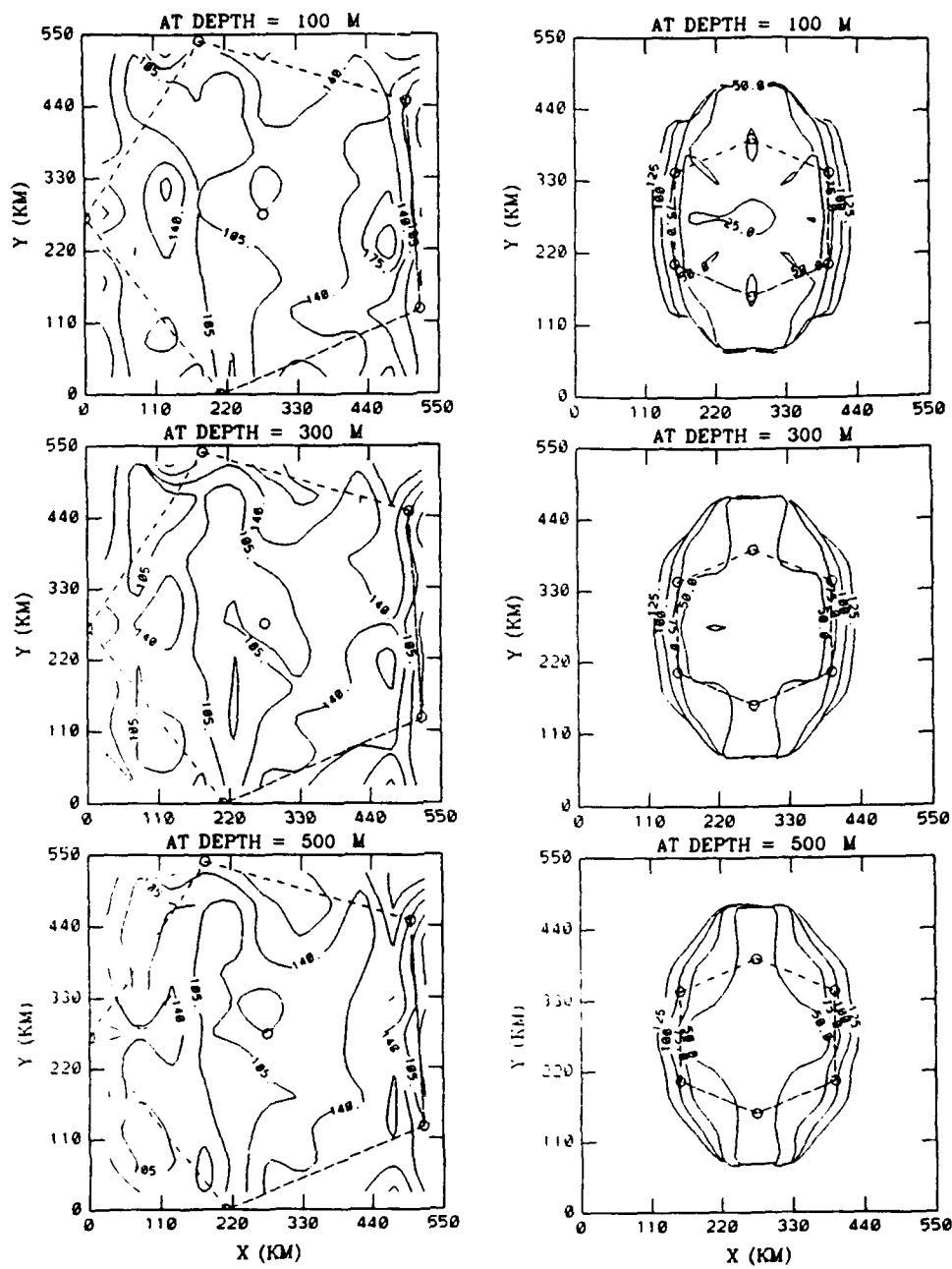
Figure 4-4 Resolution: Minimum resolution length (km) of the zonal component of January 89 current in the zonal direction for two arrays .



Array Steven

Array Harry

Figure 4-5 Resolution: Minimum resolution length (km) of the zonal component of current in the meridional direction for the two arrays



Array Steven

Array Harry

Figure 4-6 Resolution: Minimum resolution length (km) for the meridional component of current in the zonal direction for two arrays .

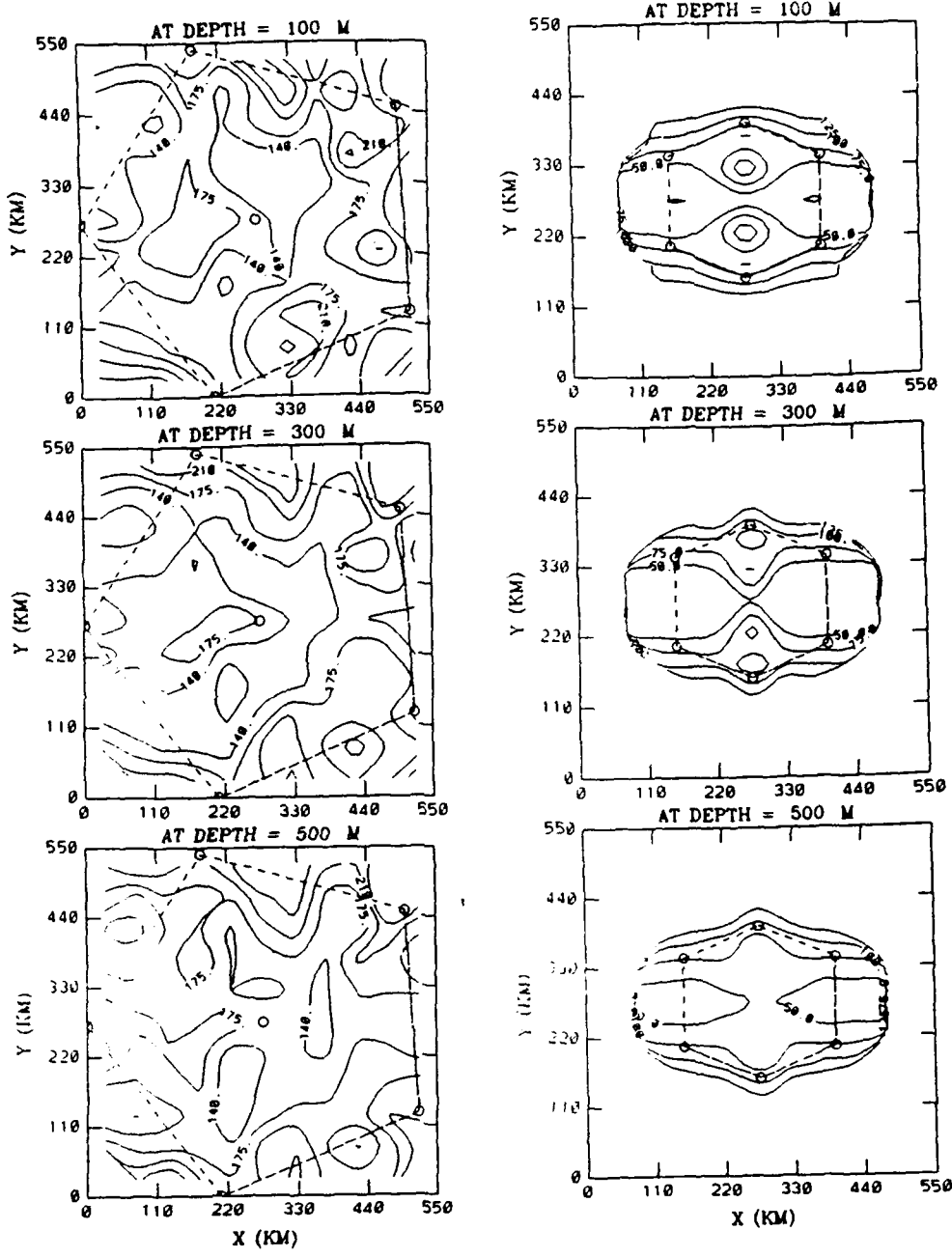
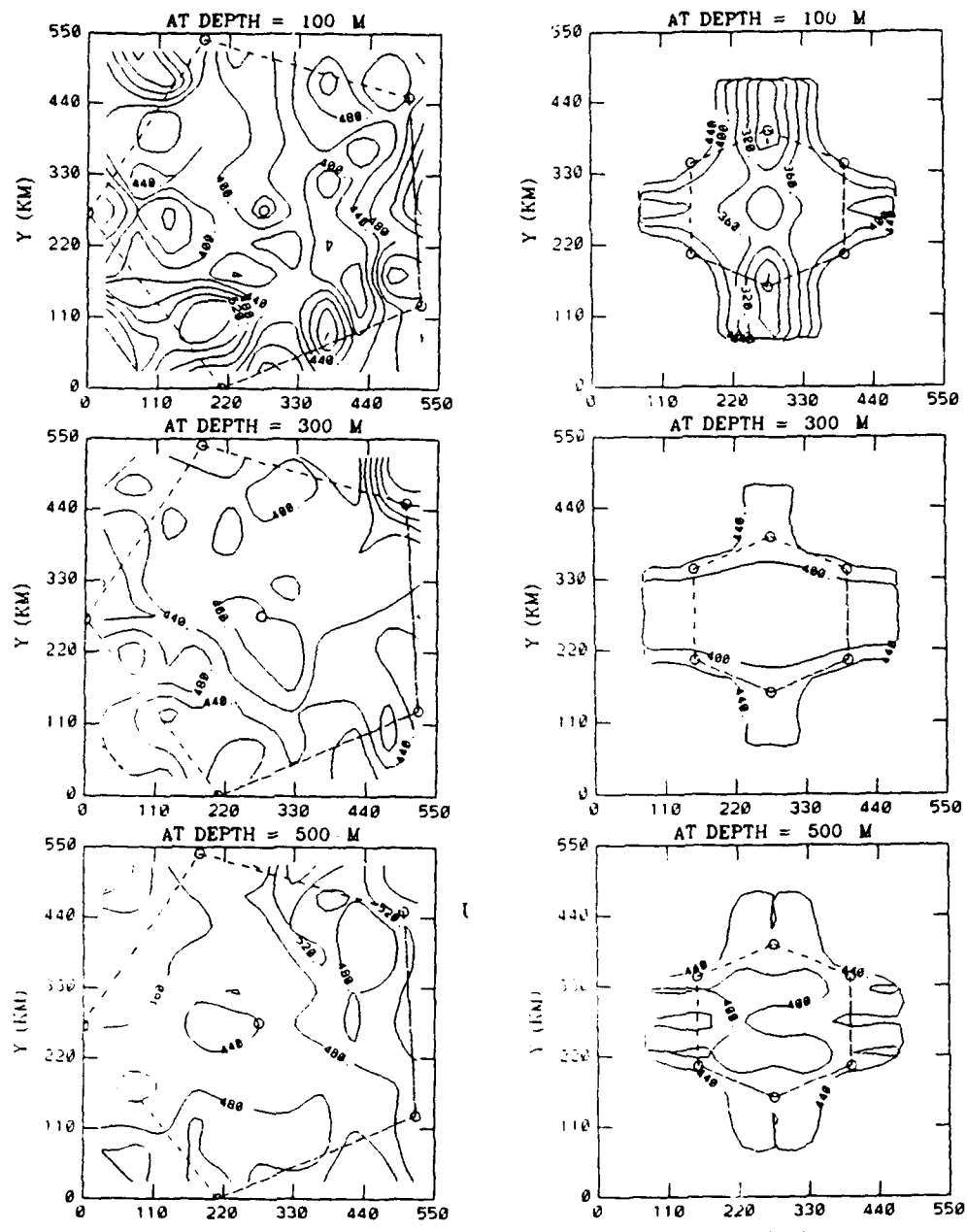


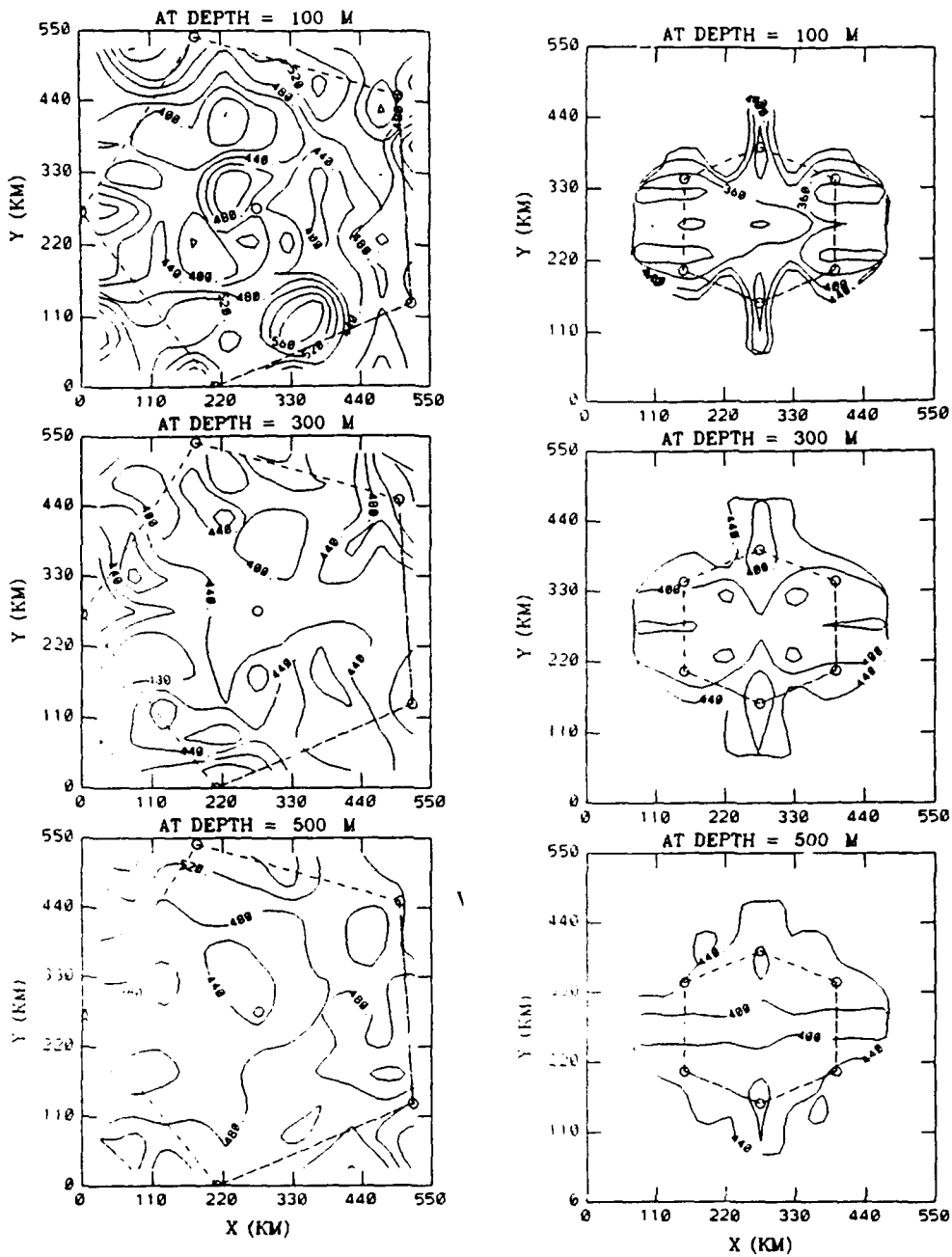
Figure 4-7 Resolution: Minimum resolution length (km) for the meridional component of current in the meridional direction for two arrays.



Array Steven

Array Harry

Figure 4-8 Resolution: Minimum Vertical resolution length (m) for the zonal component of current for two arrays.



Array Steven

Array Harry

Figure 4-9 Resolution: Minimum Vertical resolution length (m) for the meridional component of current for two arrays.

Array Harry is by far the superior array when it comes to resolution. The small array outperforms its larger competitor by a 2 to 1 margin in the horizontal and 16% in the vertical. It is obvious that increased resolution is at the expense of coverage. The compact array covers only about 25% of the area of the larger array.

Figure 4-10 is a plot of the tradeoff between minimum resolution length and array diameter, plotted for both sound speed perturbation and current. Apparent from this plot is that the sound speed perturbation field and the current field have different minimum resolution lengths. This is most pronounced near the array center. The current field has a larger minimum resolution length indicating that the array has more difficulty resolving these fields. The minimum resolution length for sound speed and current is roughly 20% of the array diameter for array Steven. There is a difference in resolution of the two unknowns in the smaller array. The minimum resolution length of sound speed is 25 km while for current it is 35 km. This means that for array Harry the minimum resolution length is 10% of array diameter for sound speed and 14% for current. Although the current field is more difficult to resolve we can improve resolution by reducing array size.

TRADE-OFF BETWEEN COVERAGE AND RESOLUTION FOR THE ESTIMATES

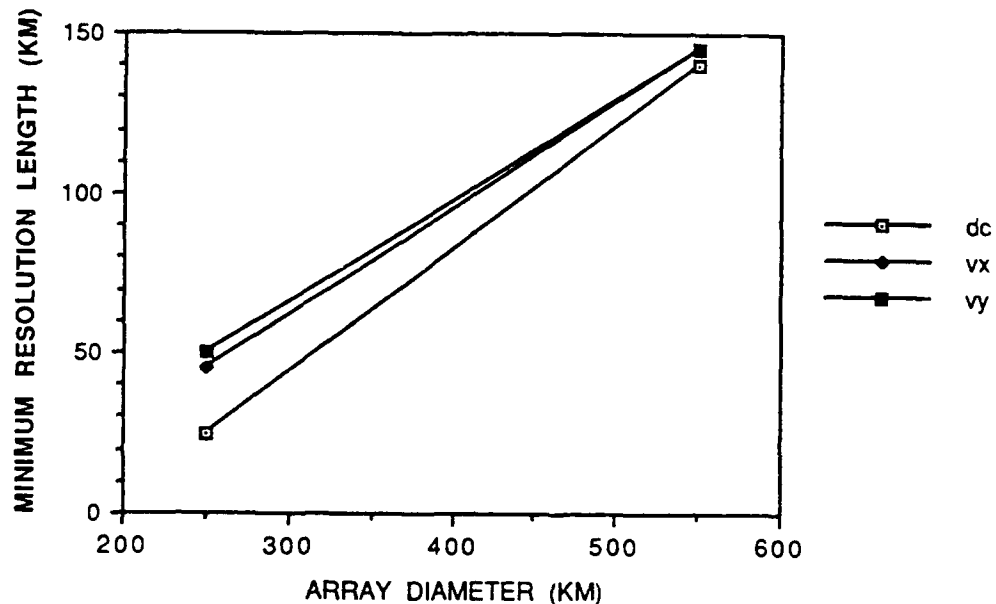


Figure 4-10 Resolution: Tradeoff between array diameter and resolution for sound speed perturbation and current fields.

Resolution length tells us whether an array has an adequate resolution to estimate the fields. An appropriate array is one that has a resolution length that is equal to or smaller than the scale of spatial variability one wants to resolve. Since our data field has a horizontal scale of 50 km, we would require a minimum resolution length of at least 50 km to adequately resolve the unknown fields. Array Harry with its small minimum resolution length satisfies this requirement.

If the resolution length is greater than 50 km, the estimated field will be a smoothed approximation of the actual field. The estimator will act as a low pass filter. This will become clearer as we examine our error analysis results in the next section.

B. ERROR

Error in the estimate is viewed in two different ways. First we examine actual errors by comparing the actual vs. estimated fields for temperature current and heat flux. We then compare the actual error with the predicted root mean square error of the estimated sound speed perturbation and current fields based on the Gauss-Markoff estimator.

1. Actual vs. Estimated Fields

a. *Theta*

Actual error in the estimate of theta was smallest. The actual and estimated fields from array Steven are compared in Figure 4-11. Comparison of the fields shows that tomography does a good job in resolving the temperature structure both horizontally and vertically. The estimate smooths some of the fine structure present in the temperature field, however this effect is subtle. Actual error is less than 1° C inside the array. Array Harry demonstrated similar performance.

In the August 89 case horizontal resolution was adequate but vertical resolution was poor. This is due to the lack of surface turning rays present in the acoustic environment.

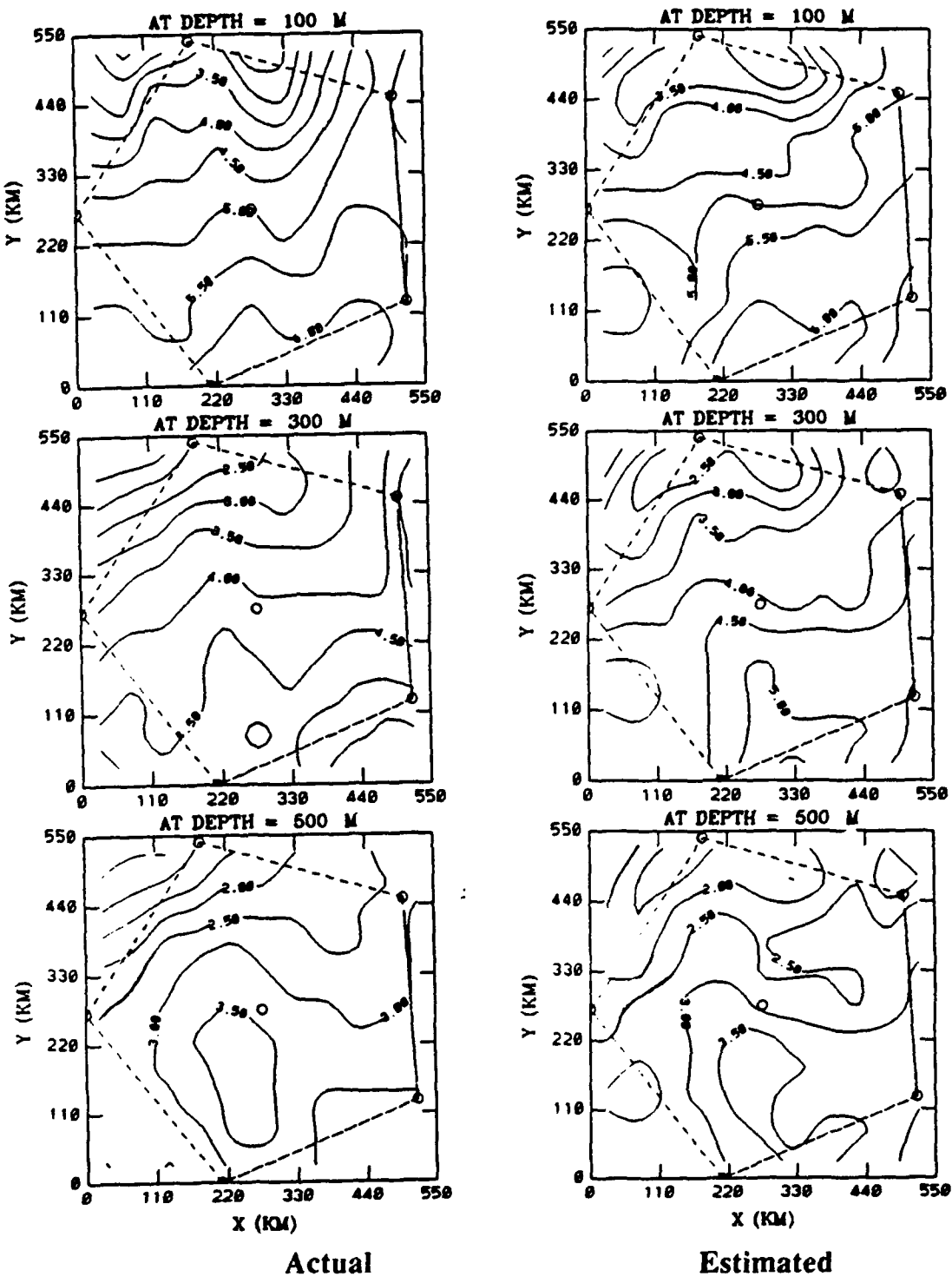


Figure 4-11 Actual vs Estimated Theta Comparison of actual vs. estimated January 89 theta fields.

Potential temperature estimates based on the compact geometry showed minor improvements. Estimates of the summer potential temperature field were not as good as the winter estimates. This again is attributed to a poorer vertical resolution.

b. Current estimates

Current is the parameter having two degrees of freedom, magnitude and direction, and a higher spatial variability and thus it is expected to be more difficult to estimate. Figures 4-12 and 4-13 show the actual vs. estimated fields for January 89 current for both arrays. The estimated fields are a smoothed version of the actual flow fields. Array Steven has the largest errors in magnitude and direction while array Harry resolves the flow quite well.

The large error in Steven can be explained in part by the nature of the a priori information we have supplied the estimator. Our estimator requires that we specify the covariance of the parameter field. We have assumed that each field is independent, isotropic, and has moderate spatial correlation. The δc parameter meets these criteria, however the current fields are quite different. Note that in Figure 4-12 the actual flow field is highly anisotropic and has a small spatial correlation. Steven does a very poor job in estimating the current especially the meridional field due to the inaccuracy of the a priori information we have specified in addition to having inadequate resolution. Both arrays tends to under-estimate the meridional field while over-estimating the zonal field. This is due to a leakage or redistribution of energy from the meridional to the zonal field caused by the inexact assumption of isotropy.

One way to overcome an inaccurate specification of a priori information is to reduce the array diameter, and this improves the horizontal resolution. Despite the inaccuracy of the a priori information array Harry does a good job in resolving the current .

The current field has a higher variability. The smoothing seen in the current estimated by array Steven is due to variations in current on a scale smaller than the minimum resolution length for that array. The smoothing of the current is significantly reduced for array Harry because the resolution length approaches the scale of the current variation. Note that temperature is resolved well in both arrays. The implication is that we must design an array to fully resolve the current structure as a minimum requirement.

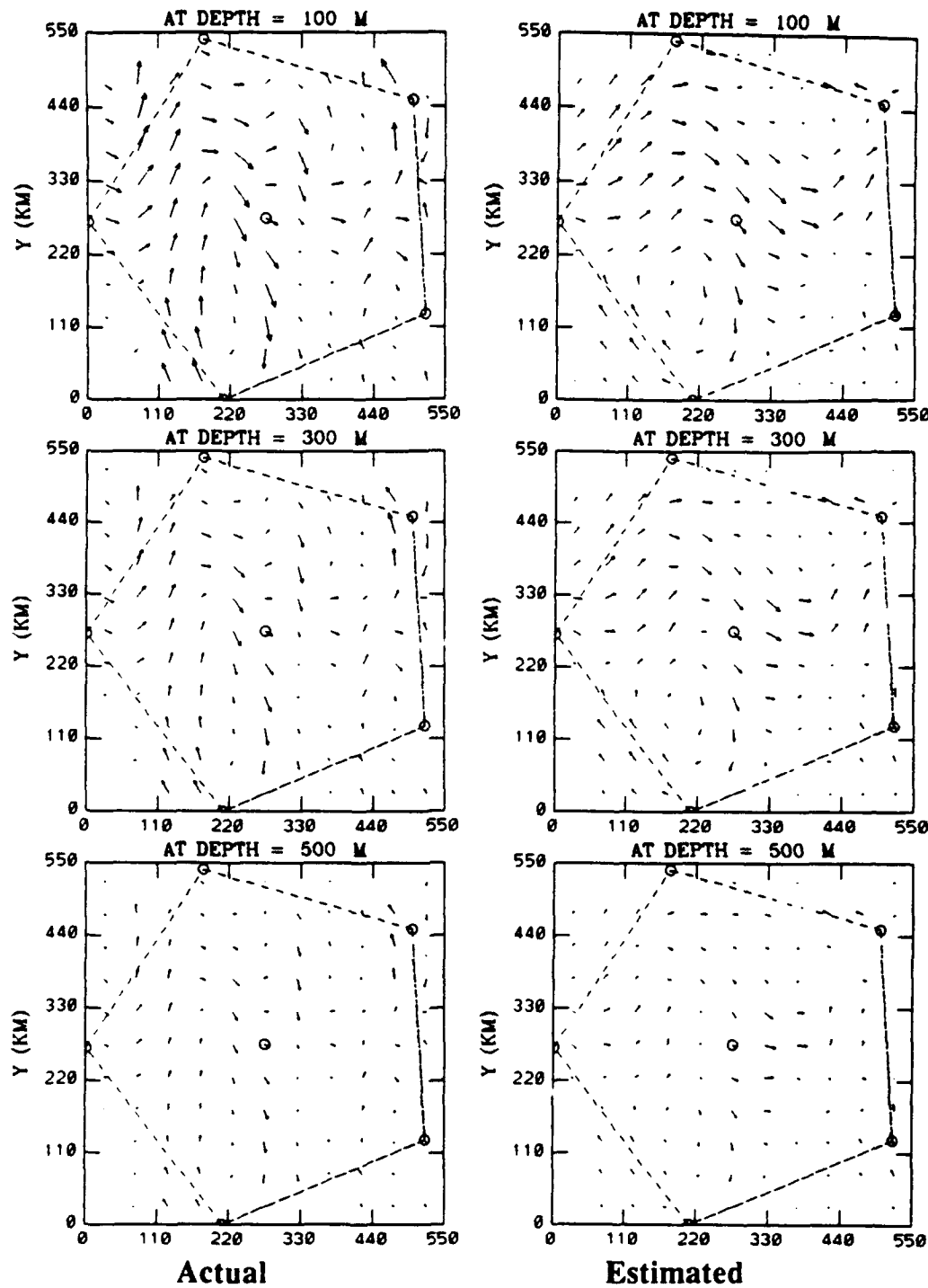


Figure 4-11 Actual vs Estimated Current: Comparison of the Actual vs estimated current for array Steven.

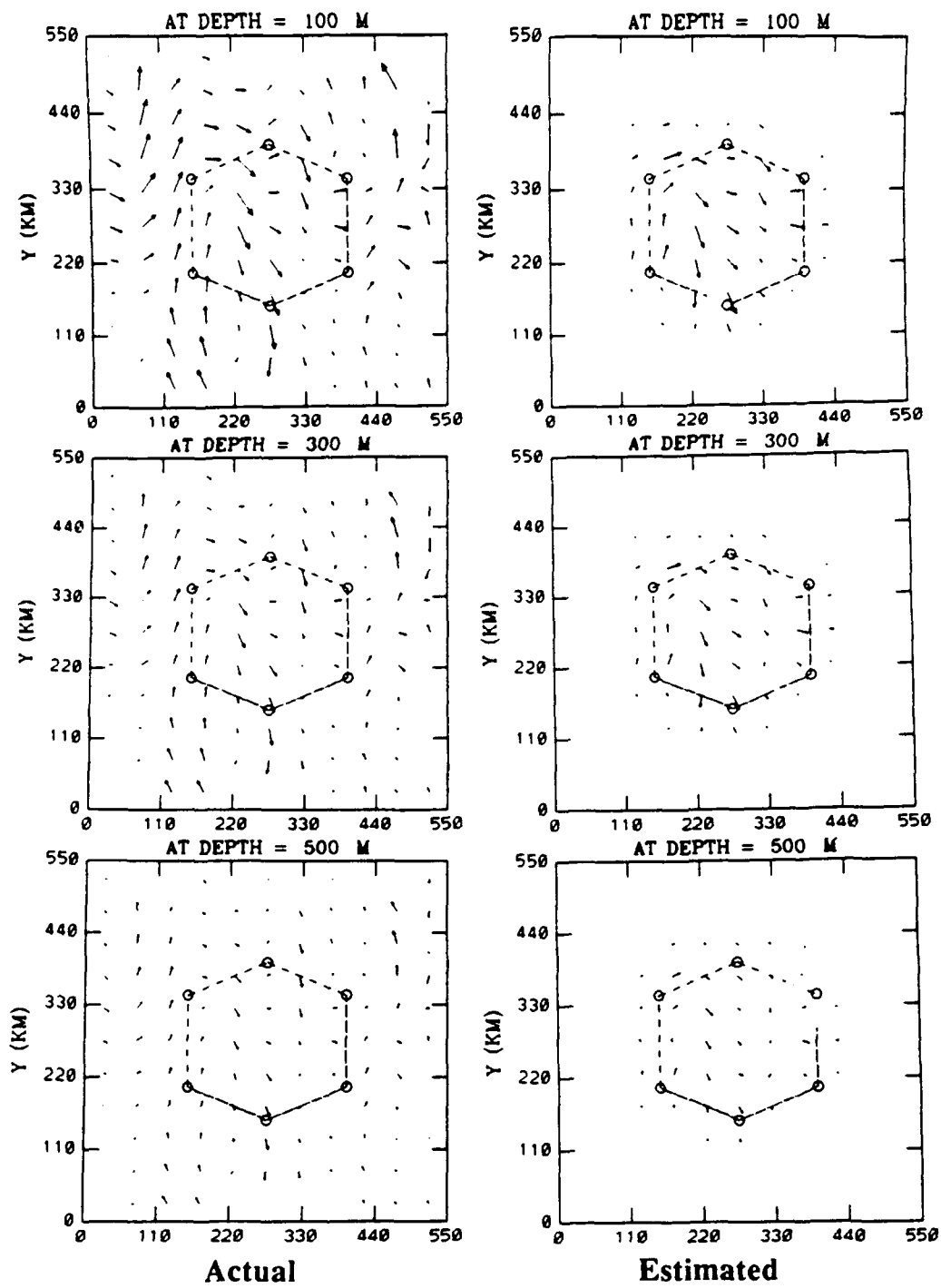


Figure 4-12 Actual vs Estimated Current: Comparison of the Actual vs estimated current for array Harry.

2. Predicted RMS Error

a. *Predicted error of the sound speed field.*

A comparison of actual and predicted error is presented in Figures 4-13 and 4-14 for both arrays. The estimator predicts less than a 50% error in the sound speed perturbation field for array Steven and less than 25% error for array Harry. Actual error for both arrays was less than predicted indicating that the actual sound speed perturbation field has a much longer correlation length than that specified.

b. *Predicted error of the current estimate*

The predicted error for the current field is presented in Figures 4-15 through 4-18. The estimator predicts an error of less than 50% for array Harry and less than 75% for array Steven. The larger error in Steven is associated with with a poorer resolution.

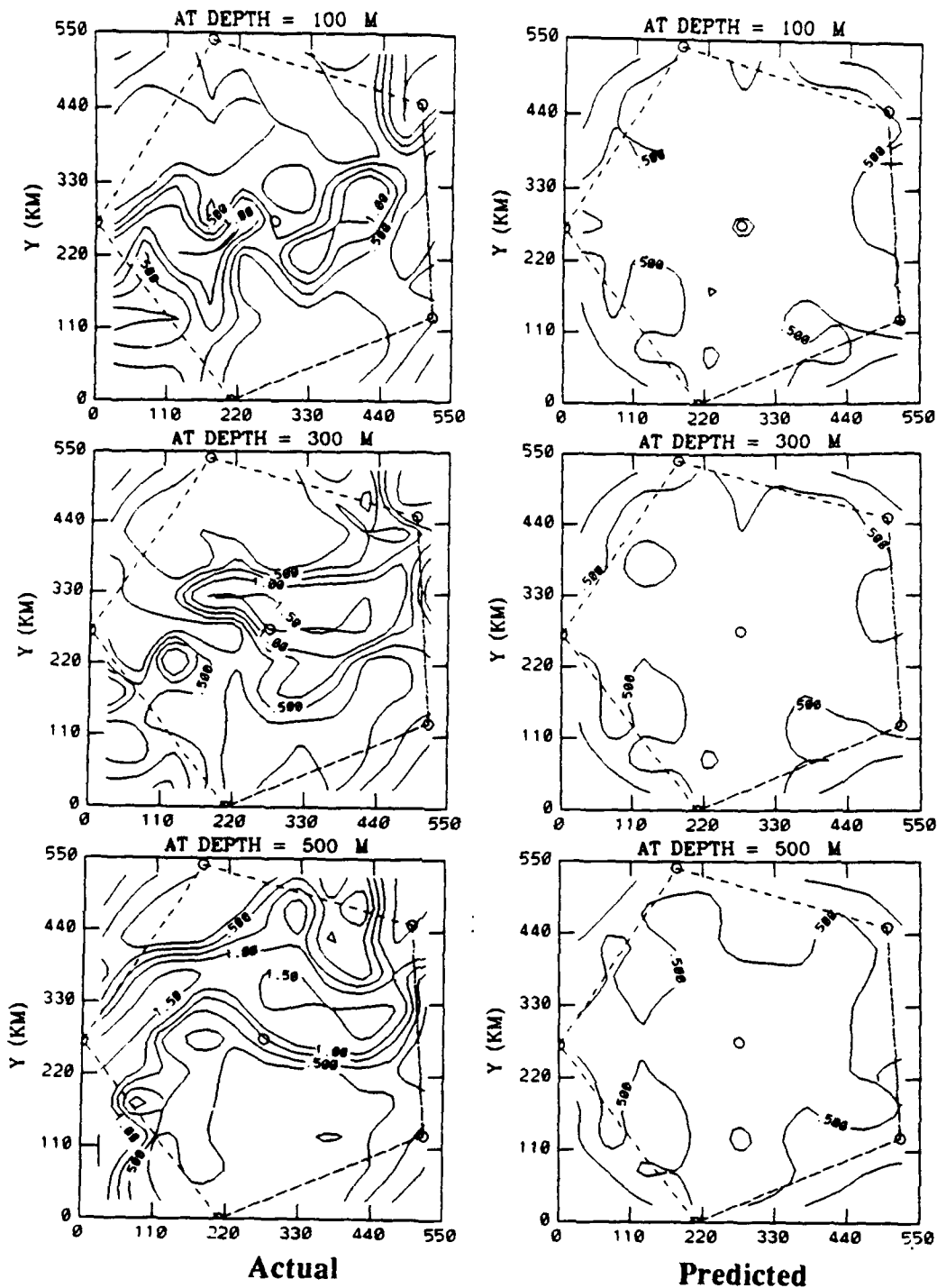


Figure 4-13 Sound Speed Error: Comparison of actual vs predicted error in the estimate of sound speed perturbation in percent by array Steven

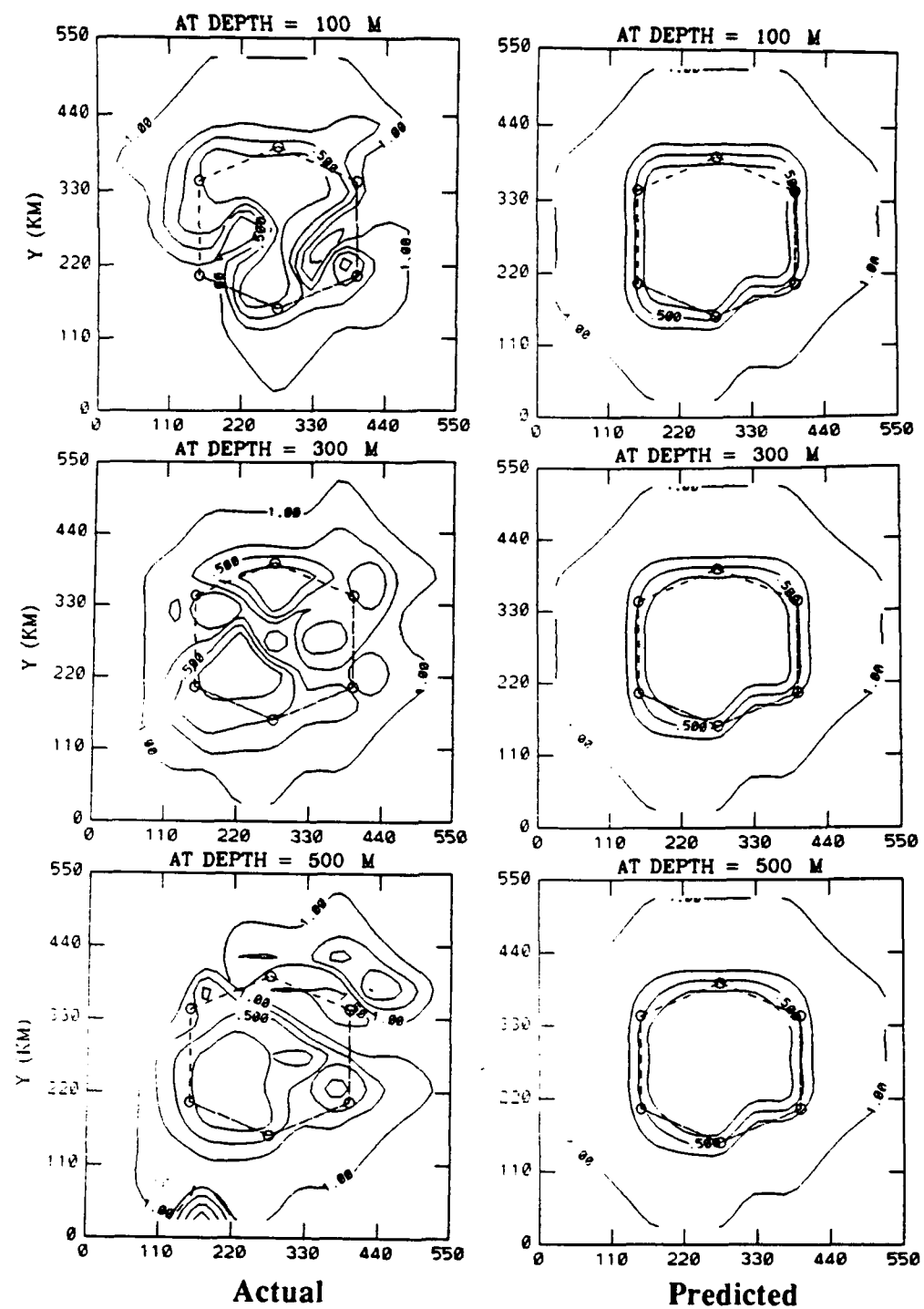


Figure 4-14 Sound Speed Error: Comparison of actual vs predicted error in the estimate of sound speed perturbation in percent by array Harry

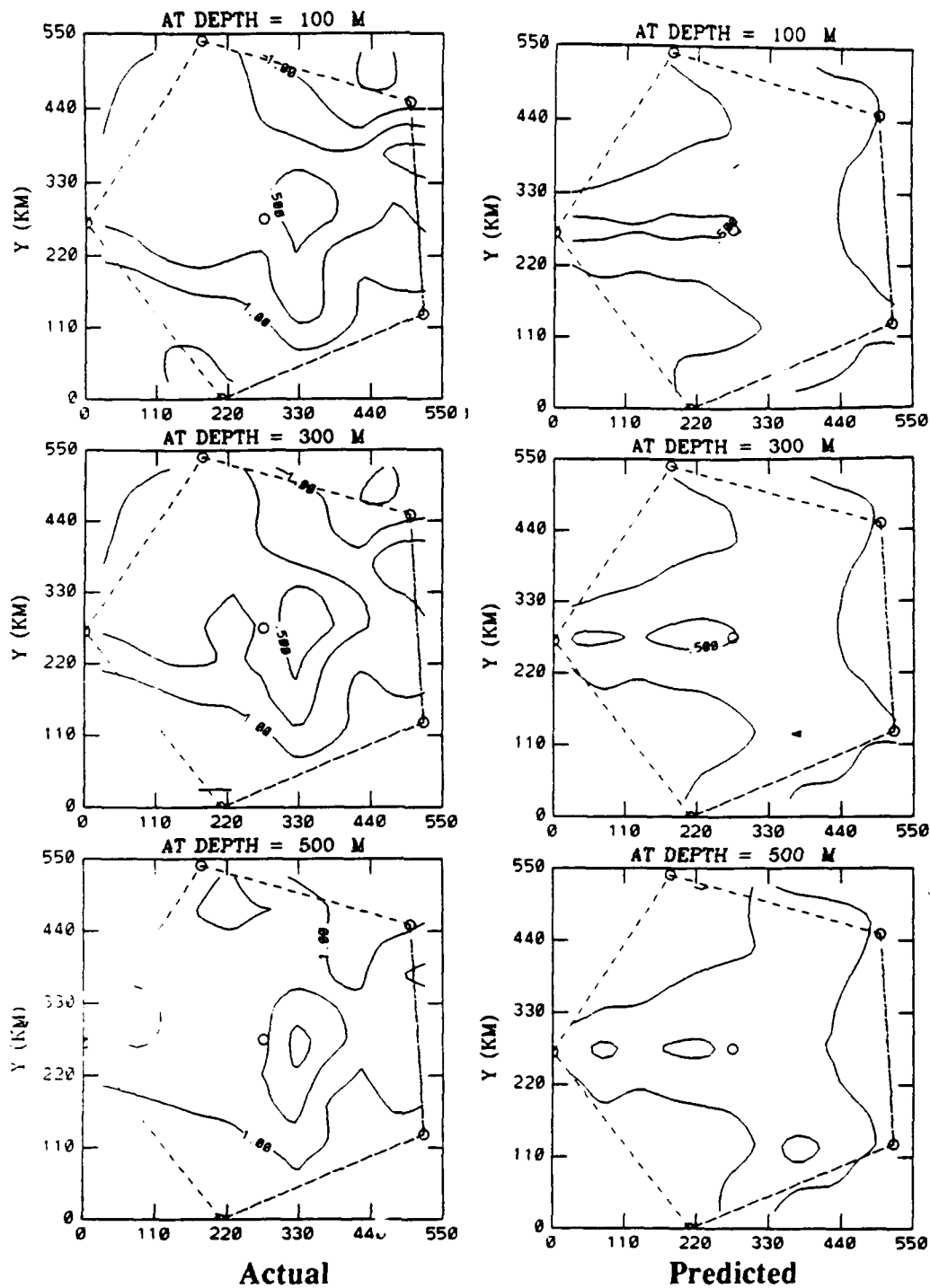


Figure 4-15 Current Error: Comparison of actual vs predicted error in the estimate of zonal current field in percent by array Steven.

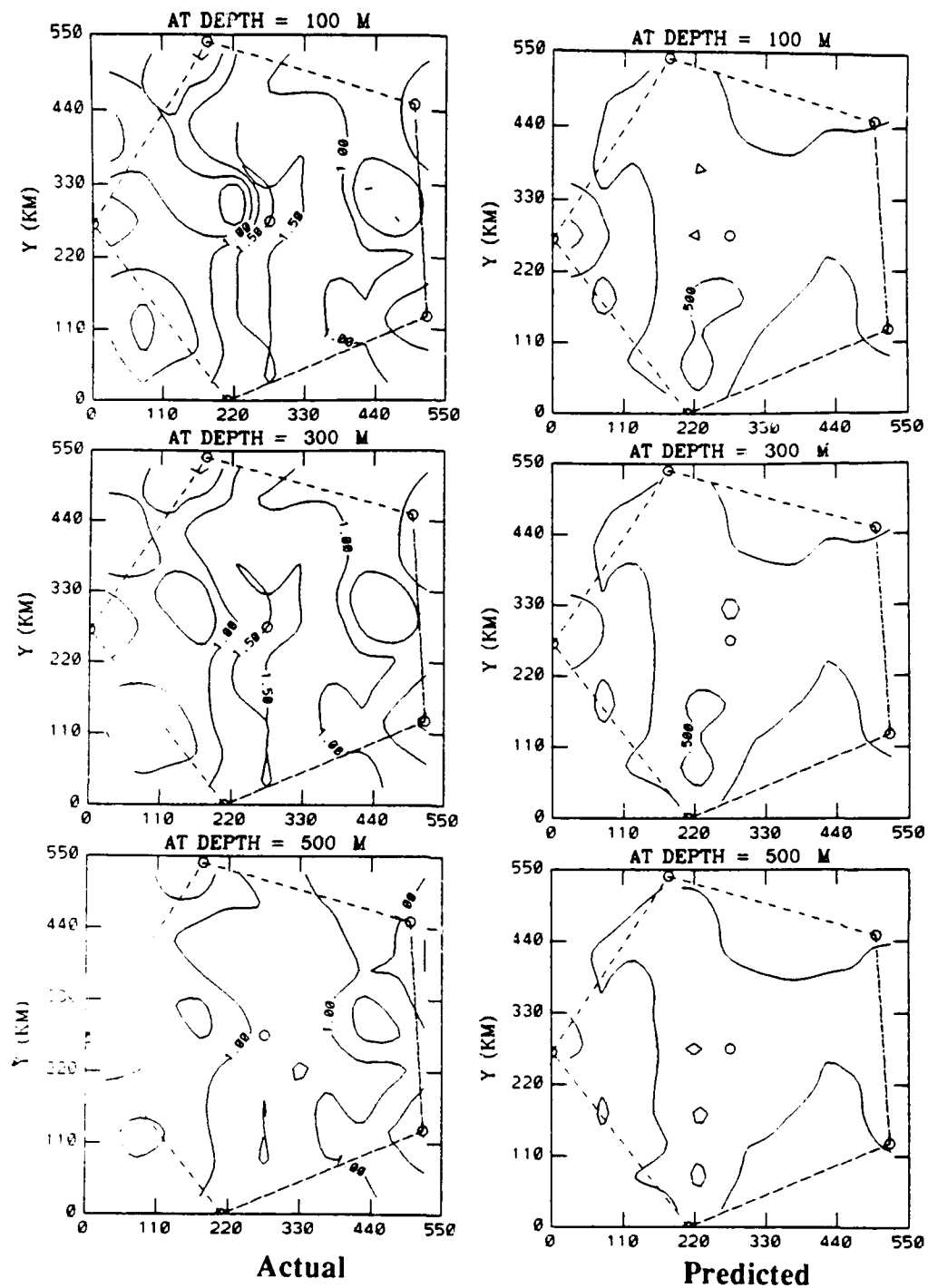


Figure 4-16 Current Error: Comparison of actual vs predicted error in the estimate of meridional current field in percent by array Steven.

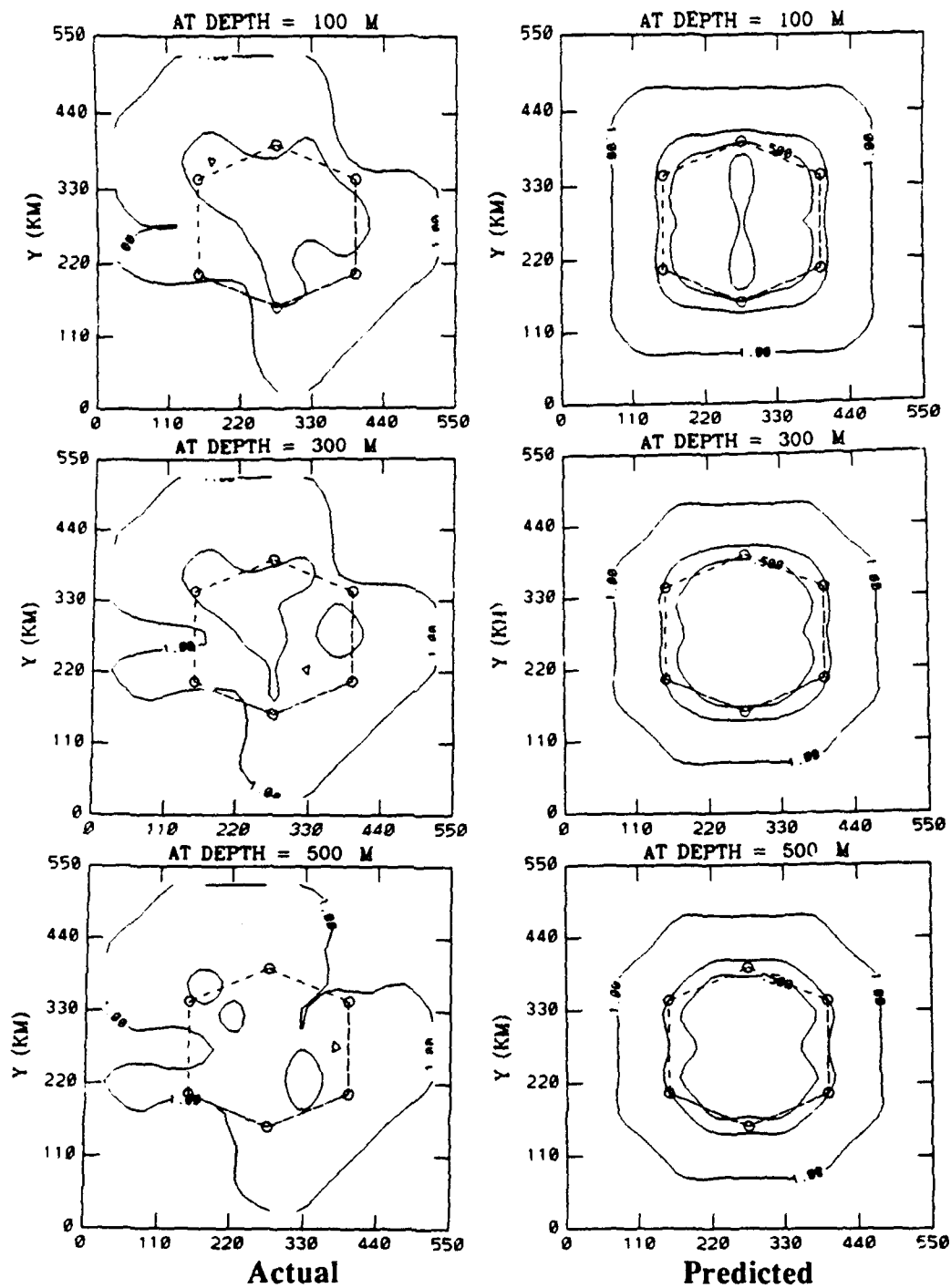


Figure 4-17 Current Error: Comparison of actual vs predicted error in the estimate of zonal current field in percent by array Harry.

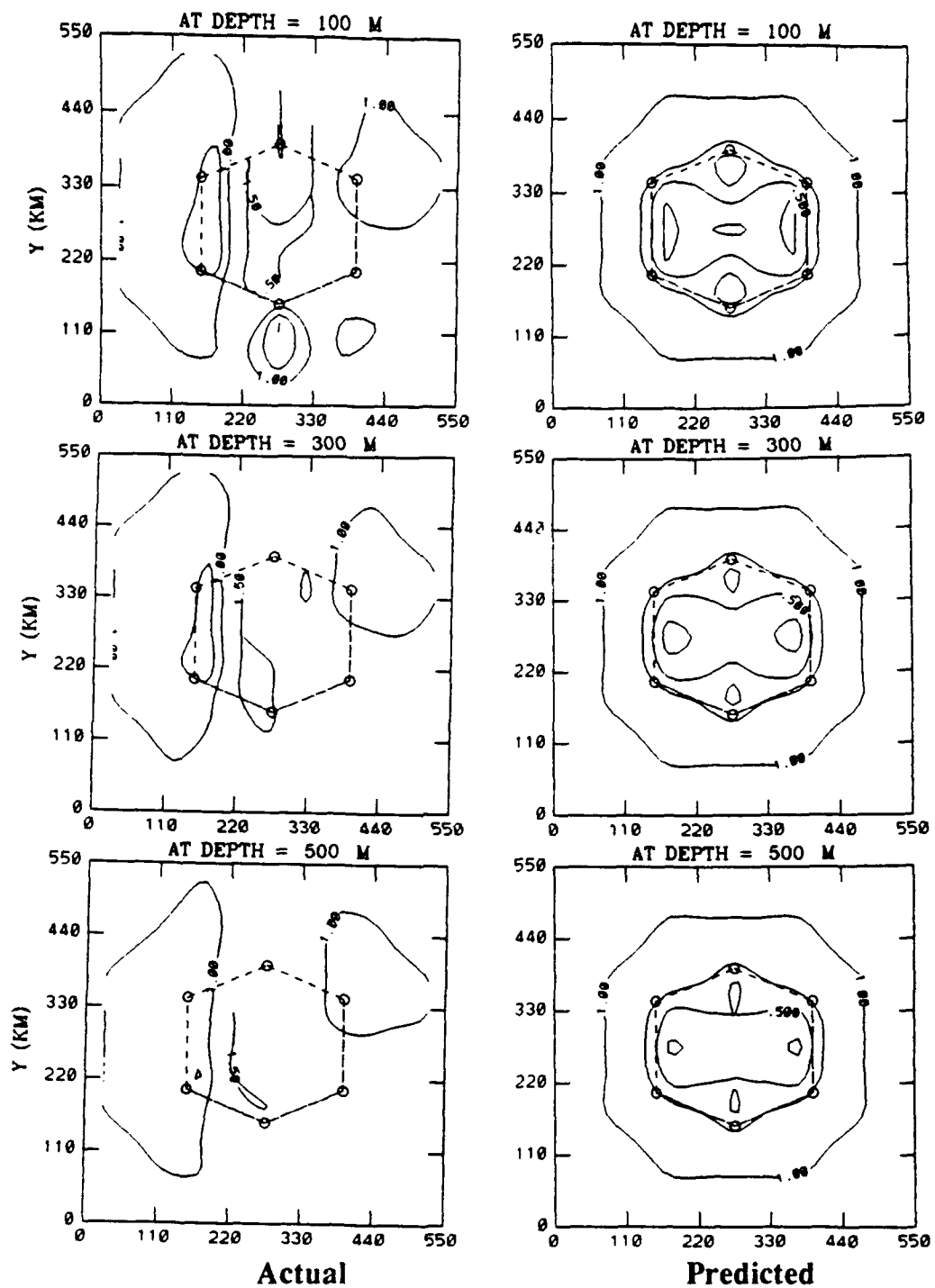


Figure 4-18 Current Error: Comparison of actual vs predicted error in the estimate of meridional current field in percent by array Harry.

C. HEAT FLUX ESTIMATES

Now we examine heat flux estimates within the array from three different perspectives, namely point estimates, depth integrated estimates and heat flux through a transect within each array.

1. Point estimates.

In Figure 4-19, we compare the actual and estimated January 89 zonal flux values at the top three layers, 100, 300, and 500 meters respectively. The estimates are based on arrays Steven and Harry, respectively. Comparing the fields, we note that array Steven tends to smooth the actual fields. In addition it also tends to under-estimate in the top layers while over-estimating the deeper layers. There is a small area near the center of the array where an over-estimation occurs. This is due to the inability of Steven to resolve the fine spatial scale.

Zonal flux estimates for array Harry compare more favorably with the actual values. Although this array covers a much smaller area the estimates are very precise, resolving well the direction and amplitude of the flux fields as shown in Figure 4-20.

Meridional estimates are compared to the actual flux values in Figure 4-21. Considerably more structure is evident in the meridional fields with a wider range between maxima and minimum. Most of the complex structure is concentrated above 500 m and tends to mirror in character the flow fields. Array Steven again tends to smooth and weaken the meridional fields. The actual error tends to be larger in the meridional estimate than in the zonal estimate.

Figure 4-22 compares the actual zonal flux fields derived from array Harry. These estimates compare well with the actual values. Within the array,

point estimates of flux are good, but degrade slightly near the boundaries. Meridional flux estimates are also handled well by array Harry as can be seen in Figure 4-23. Array Harry provides an adequate resolution of the current fields, and thus the estimate of flux is improved.

In summary we have compared the actual and estimated zonal and meridional components of heat flux at three model levels above 500 m. Point estimates of heat flux are good for the zonal case but very poor for the meridional case for array Steven. This is due primarily to the poor resolution of the meridional current field. We show a significant improvement in both zonal and meridional current estimates with array Harry due to its superior resolution.

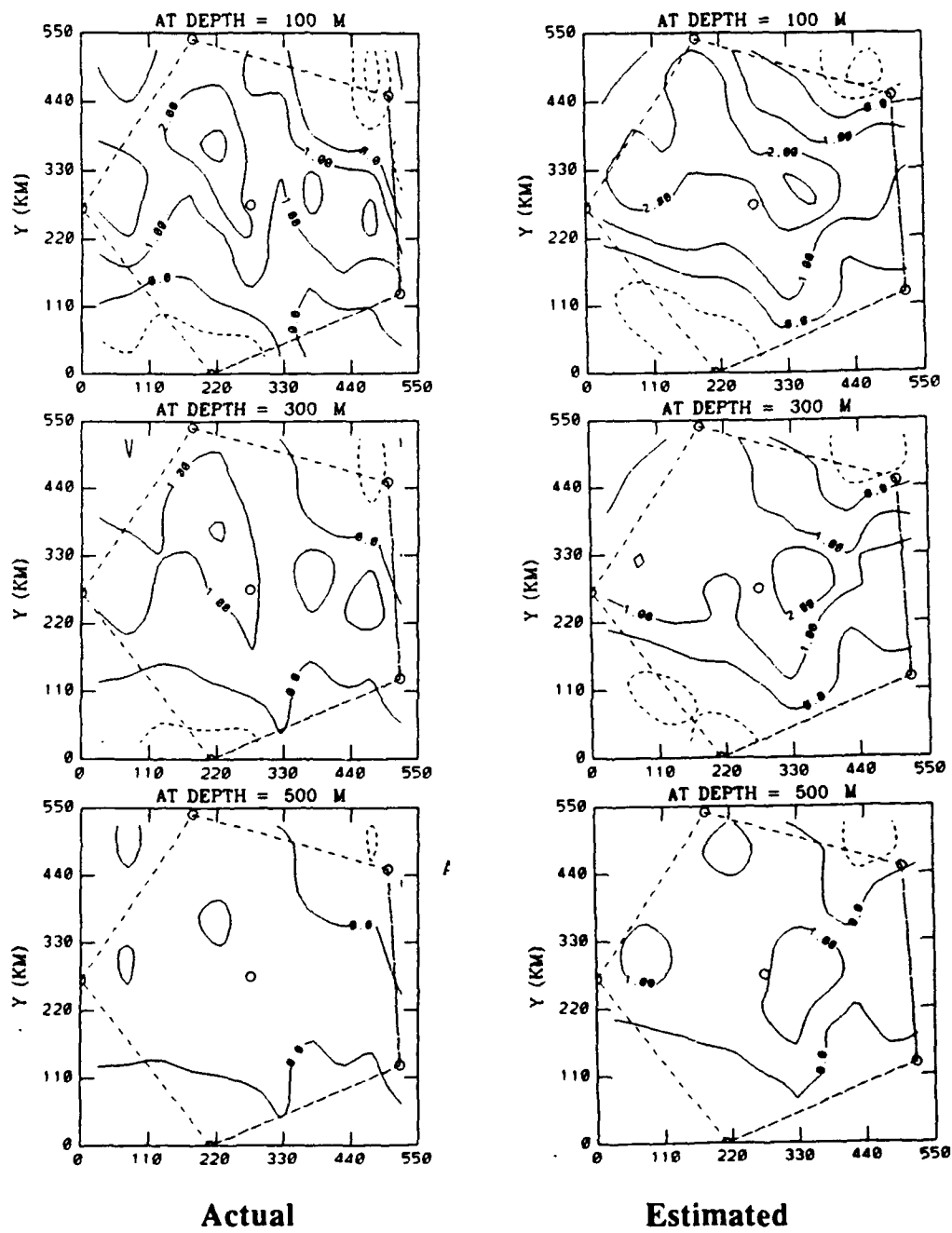


Figure 4-19 Zonal Heat Flux: Comparison of the actual January 89 zonal heat flux and its estimate generated by array Steven. Units are in $(\text{watt meter}^{-2}) \times 10^8$.

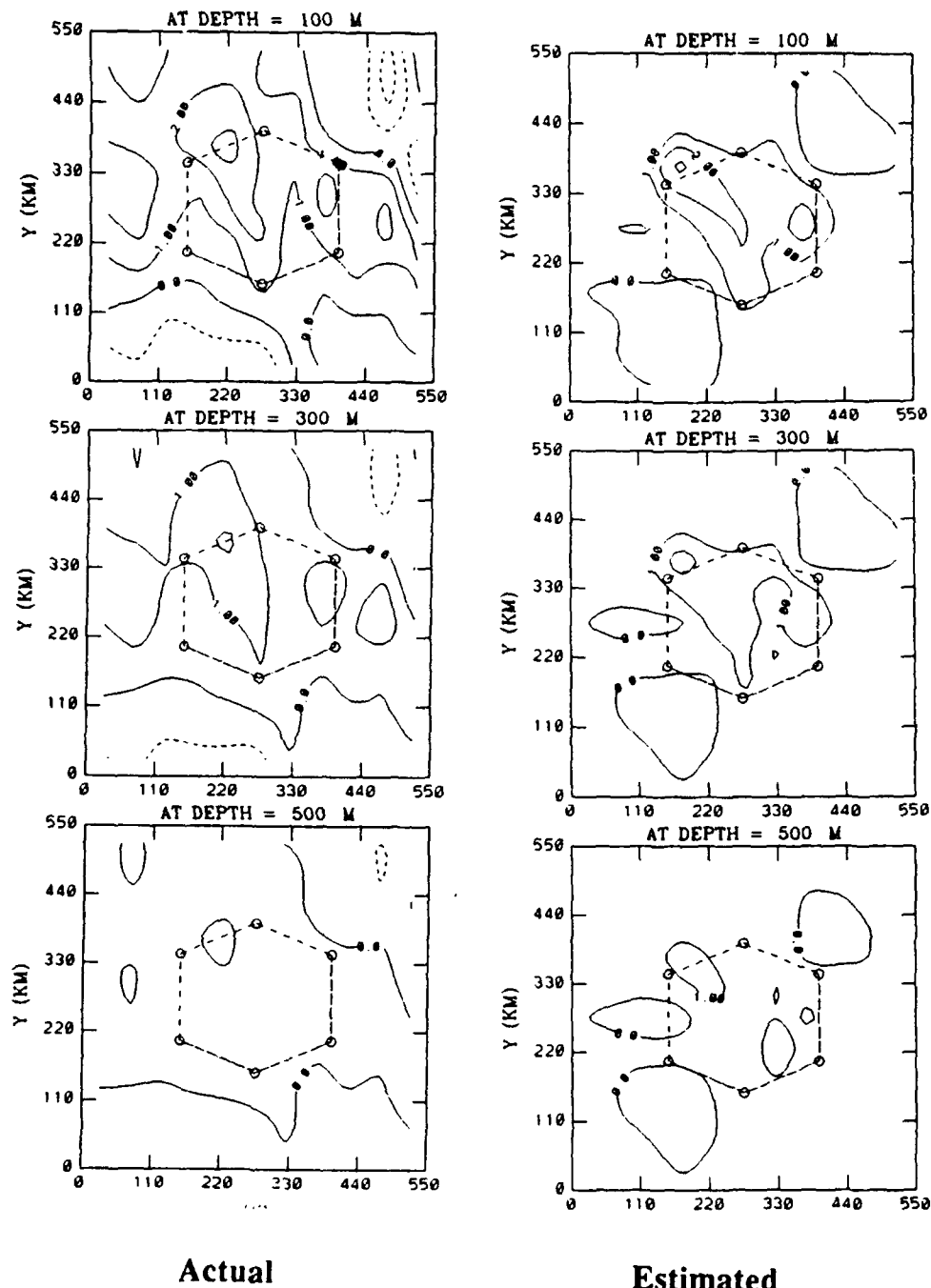


Figure 4.20 Zonal Heat Flux: Comparison of the actual January 89 zonal heat flux and its estimate generated by array Harry. Units are in (watt meter⁻²) $\times 10^8$.

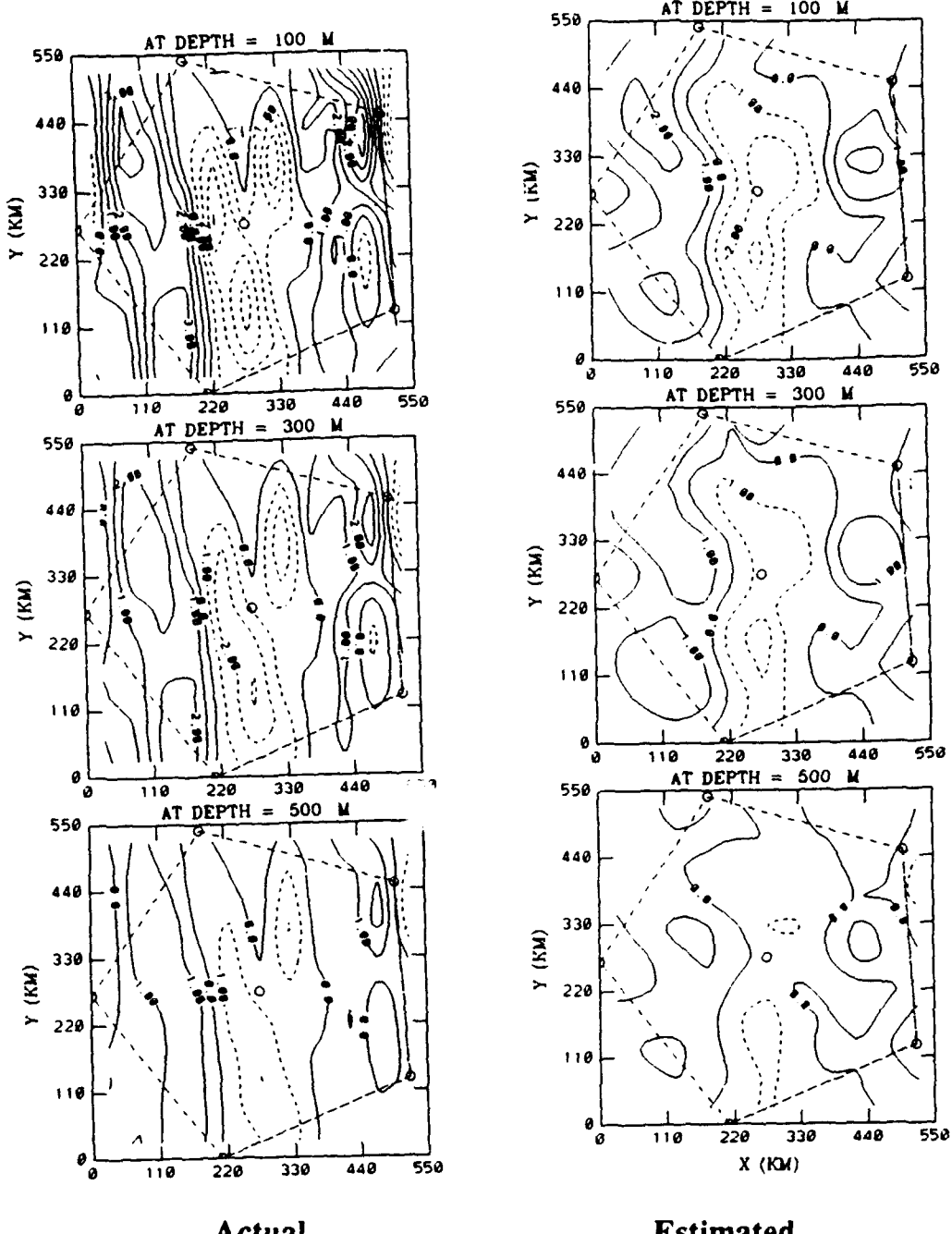


Figure 4-21 Meridional Heat Flux: Comparison of the actual January 89 meridional heat flux and its estimate generated by array Steven. Units are in $(\text{watt meter}^{-2}) \times 10^8$.

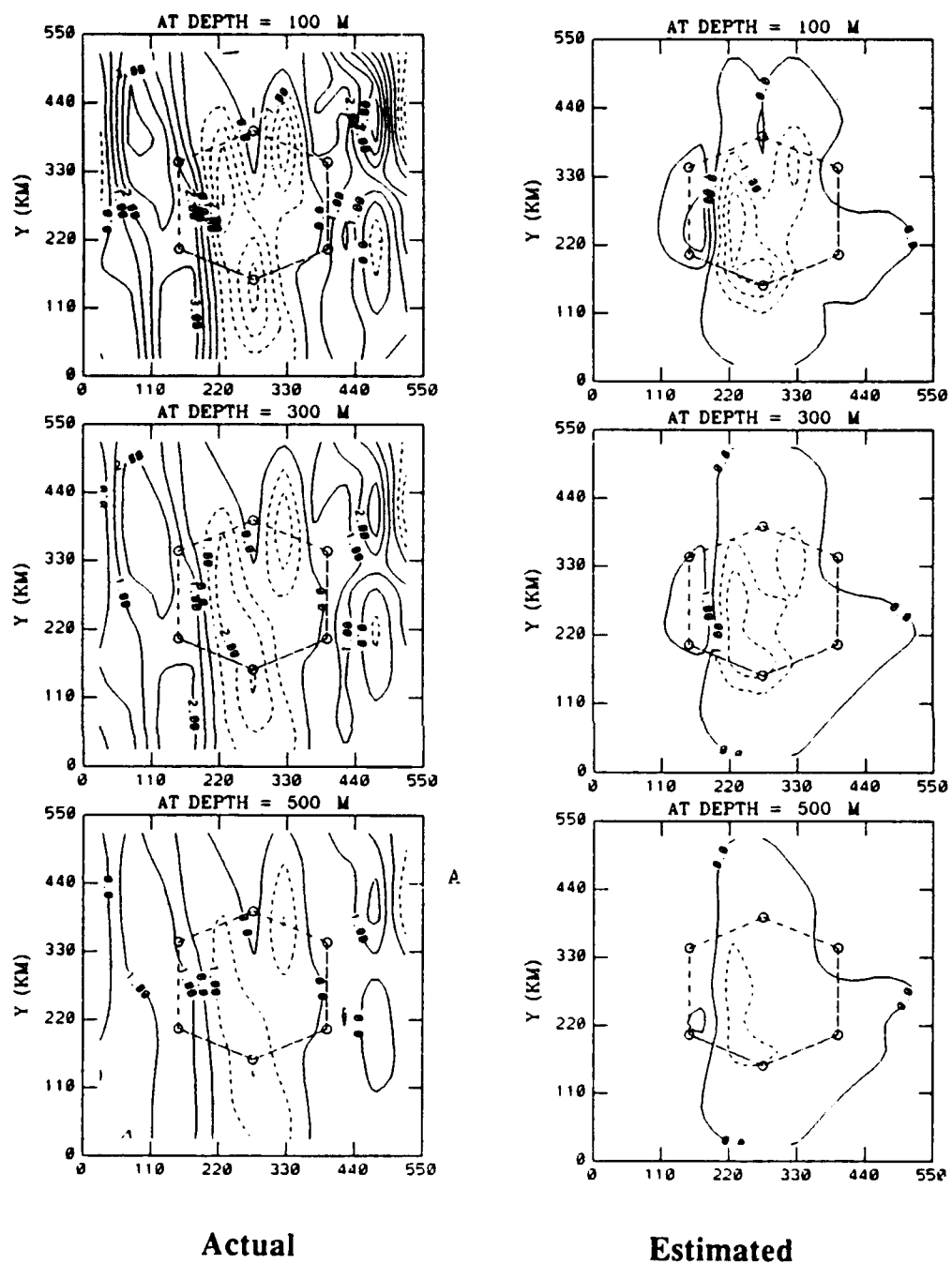


Figure 4-22 Meridional Heat Flux: Comparison of the actual January 89 meridional heat flux and its estimate generated by array Harry
Units are in (watt meter⁻²) $\times 10^8$.

2. Depth Integrated estimates

The actual depth integrated heat flux for January 89 is shown in Figure 4-23 and applies to both arrays. Large heat flux values are present in the western half of the array resulting from the warm, strong flow. Flow fields have been superimposed to show the direction of movement. The estimated depth-integrated flux field for array Steven has large errors especially near the center of the array as shown in Figure 4-24. The large positive error represents an under-estimate while the adjacent negative error represents an over-estimate. The error is caused by the fine scale of the actual fields.

In Figure 4-25 we present the January 89 depth-integrated heat flux estimated by array Harry. The estimate is superior owing to the array's fine resolving power of the flow field.

In summary we have presented a good and poor case of the tomographic estimate of heat flux in the ocean. The most significant error in the estimate of flux stems from the poor resolution of the current structure. Thus a tomographic system designed to measure heat flux must as a first priority provide good resolution of the flow field.

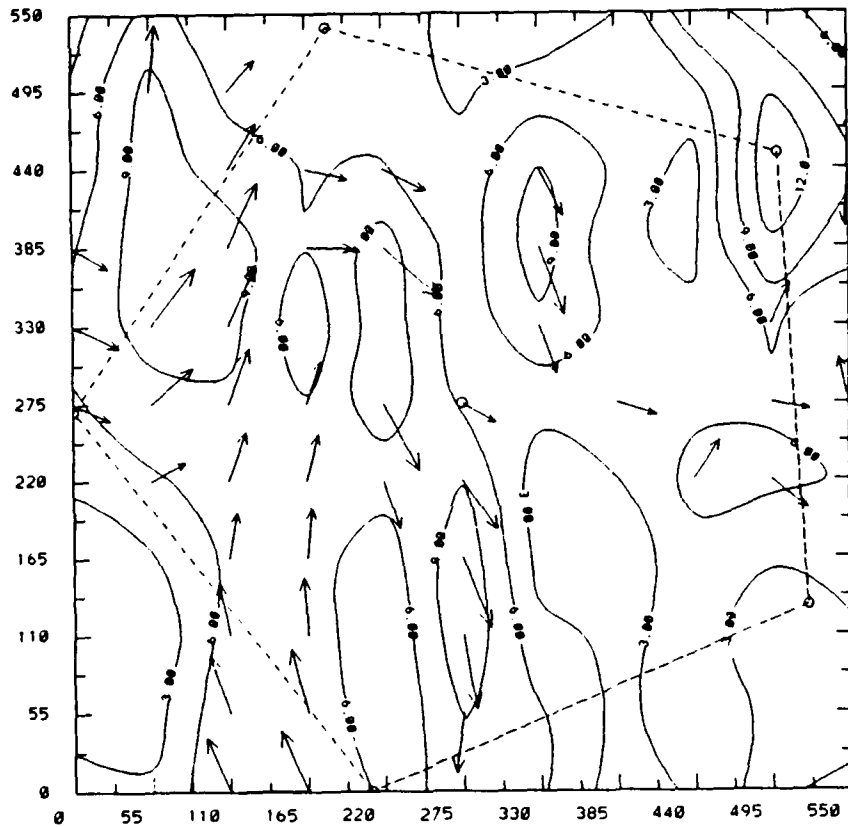


Figure 4-23 Depth Integrated Flux: Actual depth integrated January 89 heat flux for both arrays.

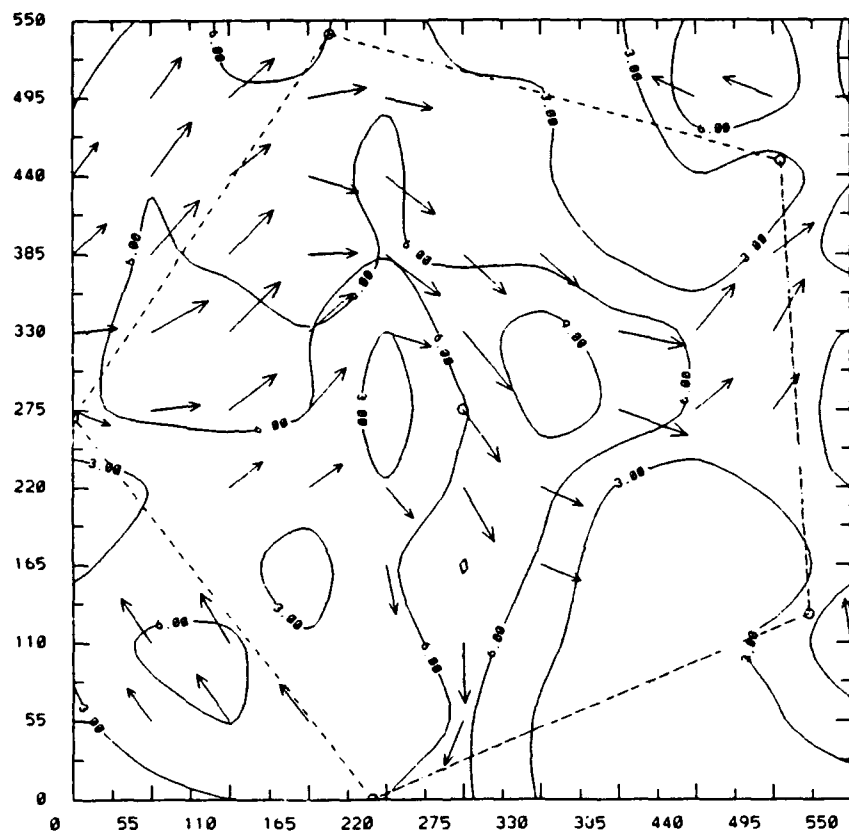


Figure 4-24 Depth Integrated Flux:Estimated depth integrated January 89 heat flux estimated by array Steven.

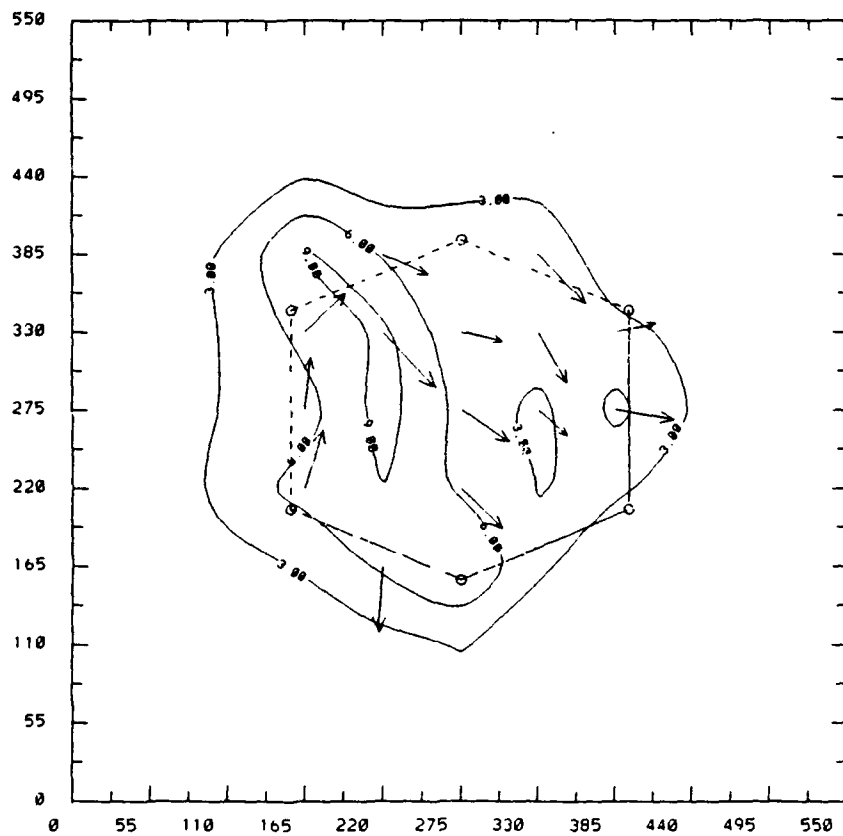


Figure 4-25 Depth Integrated Flux: Estimated depth integrated January 89 heat flux estimated by Harry.

3. Heat Flux Through a Transect

We now present heat flux estimates through a transect in each array. To form these estimates, we take a zonal and meridional transect that bisects each array and then sum the depth integrated zonal and meridional components of heat flux along that transect. The transects of both arrays coincide so that we can make a direct comparison of the estimates. A number of transects are possible within the array, but we choose the center transect in each array to standardize our approach.

Figure 4-26 displays the actual and estimated zonal heat flux through the center of the two arrays, Steven and Harry. In most locations along the transect we tend to under-estimate the zonal heat flux for array Steven. The estimates based on array Harry are far better.

Figure 4-27 gives the actual and estimated meridional heat flux through the center of the two arrays. The estimates derived from array Steven are poor showing errors in both magnitude and phase. The estimates from array Harry are much better.

Table 4.3 gives the net heat flux through transects in both arrays. Array Steven shows a 33% error in the zonal estimate while array Harry has a 4% error. Array Steven completely misses the meridional flux by being out of phase. Array Harry performs nicely with only a 9% error in the estimate of meridional flux.

TABLE 4.3 Net Heat Flux: Comparison of the actual net heat flux and the estimates from both arrays in watts x 10^8 .

Component	Steven	Harry
Zonal		
Actual	32.0	21.8
Estimate	22.3	20.8
Meridional		
Actual	5.0	-10.2
Estimate	-4.8	-9.3

Zonal Heat Flux Watt/m² x 10⁸
Through a Transect

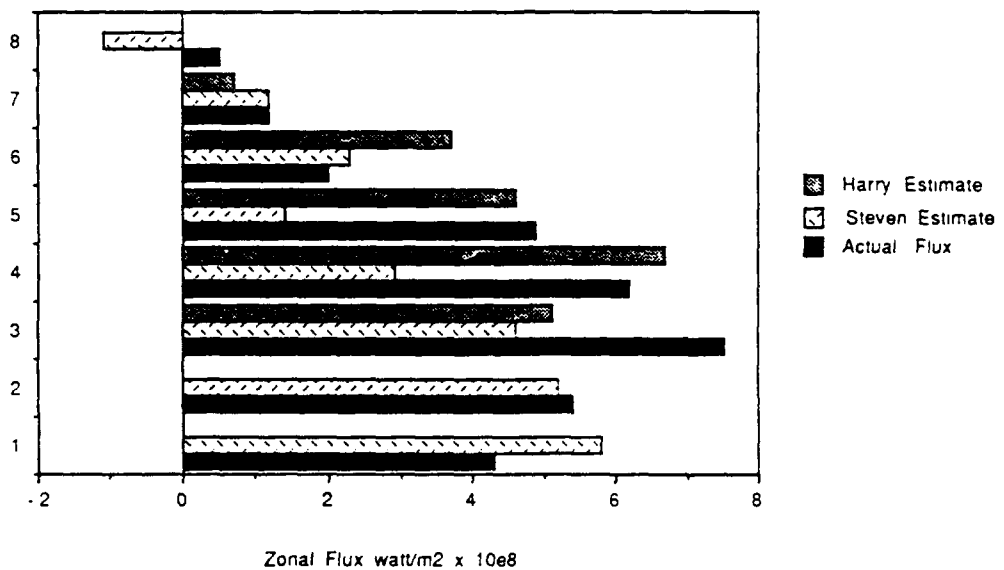


Figure 4-26 Net Zonal Flux: Net Zonal Heat Flux through a transect common to both arrays.

Meridional Heat Flux Watt/m² x 10⁸
Through a Transect

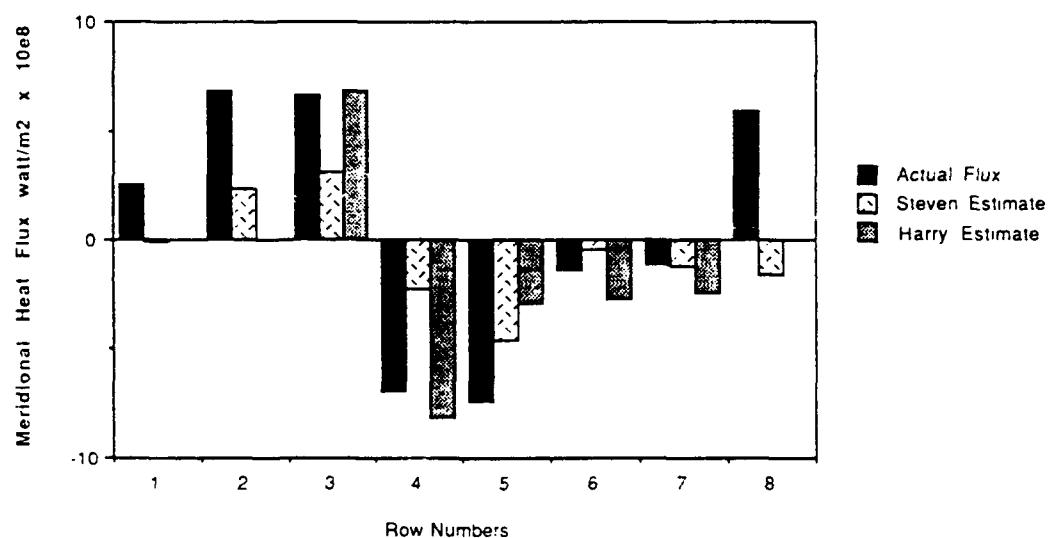


Figure 4-27 Net Meridional Flux: Net Meridional Heat Flux through a transect common to both arrays.

V. CONCLUSIONS

In this final Chapter we would like to offer a summary of our findings along with some conclusions.

A. SUMMARY

1. Covariance of the Solution

One important finding is that although the covariances specified for the sound speed perturbation and flow fields are inexact the estimates are only affected slightly providing that the system resolution is adequate. The actual error in the sound speed perturbation field was much less than predicted by the estimator. However, the current field estimates contain slightly larger errors than predicted by the estimator. This is due to the poor assumption we have made about the current fields themselves. Namely, the actual velocity fields are not isotropic. The estimator tends to redistribute the energy. As a consequence, the field is smoothed. Another problem is that we have assumed that the flow averaged 10 cm/sec at each depth when in fact the average current decreased with depth. In this case the estimator performed accordingly by under-estimating the near surface levels while over-estimating the deeper levels.

Correcting these problems is a simple matter of specifying more accurate information to the estimator through the covariance of the parameter. For example we can specify a decrease of energy with depth for the current in addition to anisotropy.

2 Acoustic Channel and Vertical Resolution

The acoustic channel also plays a significant role in the application of tomography to a given region. In this simulation, we saw the vertical resolution degrade significantly for the August 89 profile. This affects the near surface estimate of heat flux. In summer months we might rely on a technique that couples tomography with satellite derived SST data to adequately resolve the surface temperature structure.

3. Array Geometry and Horizontal Resolution

Another important consideration is the selection of an appropriate array geometry. Horizontal resolution and array geometry are inter-dependent. In this study we found that for circular arrays, rather sparse transceiver spacing was adequate in resolving temperature. However, array size had to be reduced significantly to adequately resolve the current fields. This means that to deploy an array in a flow field with a complex structure we must consider reducing the area covered or increasing the number of transceivers. The minimum spacing of transceivers is dictated by the spacing necessary to resolve current.

An asymmetrical array was also simulated to determine what improvements if any could be realized from this type of an array. The asymmetrical array with the major axis oriented with the flow did provide a slight increase in resolution. This increase in resolution, was small compared to the resolution increase from a reduction in array diameter.

4. Comparison with Conventional Techniques

Tomography compares favorably with conventional heat flux measurement techniques. We have demonstrated that the tomographic array is capable of adequately resolving both temperature and current fields over a large

area. We have shown that a six element tomographic array can adequately resolve heat flux in approximately 50,000 km² area of ocean. To provide similar coverage with direct techniques would require the deployment of 20 current meters to attain a similar resolution.

Tomography also features the advantage of providing a noise filtered measurement of current. Conventional techniques are susceptible to contamination of data from secondary sources such as tides and internal wave motion.

One disadvantage of tomography is that it is susceptible to degradation caused by failure of transceivers. Another words, failure of an array element could wipe out a large portion of data. We did not consider transceiver failure in this assessment although the topic is discussed by Kao (1989).

5. Viability of the technique

Tomography does offer a unique way of measuring the ocean's temperature and flow structures. We have seen some of it's strong points and weak points. Based on these preliminary results we have confidence in the technique and have specified ways of improving the estimate.

B. CONCLUSIONS

Acoustic tomography is a viable method of estimating ocean heat flux. It offers advantages of good spatial and temporal resolution. The method adequately resolved heat flux in this numerical simulation in the Norwegian Sea. The technique is flexible and should be adaptable to most ocean environments.

Resolution of the temperature and current fields is the key issue in this experiment. A six element circular array, 250 km in diameter, adequately resolved both temperature and current over an area 50,000 km². Heat flux

through a transect at the center of the array was estimated with a 4% error for the zonal component and a 10% error for the meridional component.

A resolution analysis of the two circular arrays revealed that the minimum resolution length is roughly 20% of the array diameter. We also found that the two unknowns, δc and V have different variability in the ocean considered and require different minimum resolution lengths. The current field is the most difficult unknown to resolve and thus it is the limiting factor in the design of a tomographic array.

Temperature fields were adequately resolved, even for a resolution length of 120 km. Current could only be resolved adequately if the resolution length was less than 50 km. Errors in the current estimates related directly to system resolution. Point flux estimates were good as long as the current was well resolved. Depth integrated estimates show that vertical resolution was adequate for the January 89 fields. The August 89 sound speed profile featured a poorer vertical resolution due to the channeling nature of the acoustic environment.

The Gauss-Markoff estimator is only optimal when supplied with correct a priori information. Estimates of current were degraded by the poor assumption made about the nature of the current fields. Estimates can be improved by specifying an anisotropic current field having an energy level that decreases with depth.

In conclusion, tomographic estimate of ocean heat flux is a technique that works and warrants further application.

REFERENCES

- Backus, G. E. and Gilbert, J. F., 1967: "Numerical Applications of a Formalism for Geophysical Inverse Problems", *Geophysical J. R. Astronomy. Society*, Vol. 13, pp. 247-76.
- Bryan, K., 1962: "Measurement of Meridional Heat Transport by Ocean Currents," *Journal of Geophysical Research*, v. 67, no. 9, pp.3403-3414.
- Bunker, A., 1976: "Computations of Surface Energy Flux and Annual Air-Sea Interaction Cycles of the North Atlantic Ocean," *Monthly Weather Review*, v. 104, pp.1122-1140.
- Cornuelle, B. D., 1985: "Tomographic Maps of the Ocean Mesoscale. Part 1: Pure Acoustics", *Journal of Physical Oceanography*, Vol. 15, pp. 133-152 .
- Chiu, C. S. and Desaubies, Y., 1987: "A Planetary Wave Analysis Using the Acoustic and Conventional Arrays in the 1981 Ocean Tomography Experiment," *Journal of Physical Oceanography*, v. 17, pp.1270-1287.
- Chiu, C. S. and Lynch, J. F., 1987: "Tomographic Resolution of Mesoscale Eddies in the Marginal Ice Zone: A Preliminary Study," *Journal of Geophysical Research*, v.92, no. C7, pp. 6886-6902.
- Clancy, R. M. and Pollak, K. D., 1983: "A Real Time Synoptic Ocean Thermal Analysis / Forecast System," *Progress in Oceanography*, v.12, pp.383-424.
- Hall, M. M. and Bryden, H. L., 1982: "Direct Estimates and Mechanisms of Ocean Heat Transport," *Deep Sea Research*, v. 29, no. 3A, pp.339-359.
- Howe B. M. and Worcester P. E., 1987: "Ocean Acoustic Tomography: Mesoscale Velocity", *Journal of Geophysical Research*, Vol. 94, No. C4, pp. 3785-3805.
- Ikeda, M., 1987: "Salt and Heat Balance in the Labrador Sea Using a Box Model," *Atmosphere-Ocean*, v. 25, no. 2,pp.197-223.
- Jung, G. H., 1952: "Note on the Meridional Transport of Energy by the Oceans," *Journal of Marine Research*, v.11, pp.139-146.

- Lynch, J. F., Spindel, R. C., Chiu, C. S., Miller, J. H., and Birdsall, T. G., 1987: "Results From the 1984 Marginal Ice Zone Experiment Preliminary Tomography Transmissions: Implications for the Marginal Ice Zone, Arctic and Surface Wave Tomography", *Journal of Geophysical Research*, Vol. 92, No. C7, pp. 6869-6885.
- Miller, J. H., Lynch, J. F. and Chiu, C. S., 1989: "Estimation of Sea Surface Spectra Using Acoustic Tomography", *The Journal of the Acoustical Society of America*, Vol. 86, No. 1, pp. 326-345.
- Munk, W. and Wunsch, C., 1979: "Ocean Acoustic Tomography: A Scheme for Large Scale Monitoring," *Deep-Sea Research* v. 26A, pp. 123-161.
- Munk, W. and Wunsch, C., 1983: "Ocean Acoustic Tomography: Rays and Modes," *Journal of Geophysical Research*, v. 21, no. 4, pp. 777-793.
- Naval Postgraduate School, Unclassified, Letter: Proposal for Research, Office of Naval Research, Subject, 1989: "Feasibility Study for a Norwegian Continental Shelf- Barents Sea Acoustic Tomography Experiment".
- Oort, A. H. and Vonder Haar, T. H., 1976: "On the Observed Annual Cycle in the Ocean-Atmosphere Heat Balance over the Northern Hemisphere," *Journal of Physical Oceanography*, v. 6, pp. 781-800.
- Parker, R. L., 1977: "Understanding Inverse Theory," *Annual Review of Earth and Planetary Science*, v. 5, pp. 35-64.
- Spindel, R. C., 1985: "Signal Processing in Ocean Tomography," *Adaptive Methods in Underwater Acoustics*, D. Reidel, Boston, pp. 687-710.
- Sverdrup, H. U., 1957: "Oceanography," *Handbook der Physik*, v.48, Springer-Verlag, Berlin, pp. 608-670.
- Vonder Haar, T. H. and Oort, A. H., 1973: "New Estimate of Annual Poleward Energy Transport by Northern Hemisphere Oceans," *Journal of Physical Oceanography*, v. 2, pp. 169-172.

INITIAL DISTRIBUTION LIST

	No. Copies
1. Defense Technical Information Center Cameron Station Alexandria, Virginia 22304-6145	2
2. Library, Code 0142 Naval Postgraduate School Monterey, California 93943-5100	2
3. Chairman (Code Oc/Co) Department of Oceanography Naval Postgraduate School Monterey, CA 93943-5000	1
4. Chairman (Code Me/Re) Department of Meteorology Naval Postgraduate School Monterey, CA 93943-5000	1
5. Professor Curtis A. Collins (Code Oc/Co) Department of Oceanography Naval Postgraduate School Monterey, CA 93943-5000	1
6. Professor Ching-Sang Chiu (Code Oc/Ci) Department of Oceanography Naval Postgraduate School Monterey, CA 93943-5000	5
7. Professor James H. Miller (Code Ee/Mr) Department of Oceanography Naval Postgraduate School Monterey, CA 93943-5000	1
8. Director Naval Oceanography Division Naval Observatory 34th and Massachusetts Avenue NW Washington, DC 20390	1

- | | |
|---|---|
| 9. Commander | 1 |
| Naval Oceanography Command | |
| Stennis Space Center | |
| Bay St. Louis, MS 39529-5000 | |
| 10. Commanding Officer | 1 |
| Naval Oceanographic Office | |
| Stennis Space Center | |
| Bay St. Louis, MS 39522-5001 | |
| 11. Commanding Officer | 1 |
| Fleet Numerical Oceanography Center | |
| Monterey, CA 93940-5005 | |
| 12. Commanding Officer | 1 |
| Naval Ocean Research and Development Activity | |
| Stennis Space Center | |
| Bay St. Louis, MS 39522-5004 | |
| 13. Director | 1 |
| Naval Oceanographic and Atmospheric | |
| Research Laboratory (West) | |
| Monterey, CA 93943-5006 | |
| 14. Chairman, Oceanography Department | 1 |
| U. S. Naval Academy | |
| Annapolis, MD 21402 | |
| 15. Chief of Naval Research | 1 |
| 800 N. Quincy Street | |
| Arlington, VA 22217 | |
| 16. Office of Naval Research (Code 420) | 1 |
| Naval Ocean Research and Development Activity | |
| 800 N. Quincy Street | |
| Arlington, VA 22217 | |
| 17. Scientific Liason Office | 1 |
| Office of Naval Research | |
| Scripps Institution of Oceanography | |
| La Jolla, CA 92037 | |

- | | |
|-------------------------------------|---|
| 18. Library | 1 |
| Scripps Institution of Oceanography | |
| P.O. Box 2367 | |
| La Jolla, CA 92037 | |
| 19. Library | 1 |
| Department of Oceanography | |
| University of Washington | |
| Seattle, WA 98105 | |
| 20. Lieutenant Commander Tim Barock | 1 |
| USS Kitty Hawk (CV-63) | |
| Fleet Post Office | |
| New York, New York 09535-2770 | |
| 21. Mr. Mike Clancy | 1 |
| Ocean Models Division | |
| Fleet Numerical Oceanography Center | |
| Monterey, CA 93940-5005 | |
| 22. Dr. James Lynch | 1 |
| Woods Hole Oceanography Institution | |
| Woods Hole, MA 02543 | |
| 23. Mr. Donald E. Barock | 1 |
| #8 Burnt Pines | |
| Northport, AL 35476 | |
| 24. Dr Beth Chertock | 1 |
| NOAA - WPL | |
| 325 Broadway | |
| Boulder, CO 80303-3328 | |